

Automatic extraction of patient set up features using portal images

by

Keyvan Jabbari

A thesis presented to the Faculty of Graduate Studies of University of
Manitoba in partial fulfillment of the requirements for the degree of

MASTER OF SCIENCE

Department of Physics and Astronomy

University of Manitoba

Winnipeg, Manitoba, Canada

©August 2004

**THE UNIVERSITY OF MANITOBA
FACULTY OF GRADUATE STUDIES

COPYRIGHT PERMISSION**

**Automatic extraction of patient set up
features using portal images**

BY

Keyvan Jabbari

**A Thesis/Practicum submitted to the Faculty of Graduate Studies of The University of
Manitoba in partial fulfillment of the requirement of the degree
Of
MASTER OF SCIENCE**

Keyvan Jabbari © 2004

Permission has been granted to the Library of the University of Manitoba to lend or sell copies of this thesis/practicum, to the National Library of Canada to microfilm this thesis and to lend or sell copies of the film, and to University Microfilms Inc. to publish an abstract of this thesis/practicum.

This reproduction or copy of this thesis has been made available by authority of the copyright owner solely for the purpose of private study and research, and may only be reproduced and copied as permitted by copyright laws or with express written authorization from the copyright owner.

/

ABSTRACT

Electronic Portal Imaging Devices (EPID's) may be used for on-line verification in processes involved in the treatment of cancer. A portal image can be registered spatially with its reference image to determine whether the patient is set up in the prescribed treatment position. Visual comparison of portal images is often complicated and automated methods will enable the use of the EPID's ability to improve the efficiency of the treatment verification.

In the first part of this work the properties of the Fourier transform of the image have been used to align the portal image with the reference image. By correlating the log polar representation of the Fourier transform of the image we can recover the transformation parameters from two images that differ by a Rotation-Scale-Translation. We have shown that for a portal image of the pelvis we are able to extract the scale factor from 0.8 to 1.2 and rotation factor between 0° to 45° with an accuracy better than 3.6 %, and 3° , respectively. The translation factor can be extracted with an accuracy of ± 1 pixel as long as the rotation factor is recovered with an accuracy of better than $\pm 5^\circ$.

In the second part of this work we have evaluated the possibility of detecting out-of-plane rotation using a single portal image. Out-of-plane rotation results in an apparent distortion of anatomy in the portal image. This distortion can be mathematically predicted with the magnification varying at each point in the image. While an equal change of magnification in both dimensions results from an incorrect SSD setup, a variation of magnification in only one dimension is due to an out-of-plane rotation. A technique similar to that, used for in plane transforms, can be used to calculate the out-of-plane rotation. Correlating the Fourier Transform of the portal image on a log scale with that of the reference image enables the out-of-plane rotation to be automatically extracted from a single portal image.

This technique is able to identify out-of-plane rotations between 2° and 20° with an accuracy of $\pm 2^\circ$. The ability to detect out-of-plane rotations with a single image will enhance our ability to quickly and accurately account for both in-plane and out-of-plane set-up errors.

Acknowledgment

I would like to thank my advisor Dr Stephen Pistorius for his guidance and motivation.

His great ideas in critical situations led to much progress in this project.

I would also like to thank Dr. Boyd McCurdy who always was happy to help me and answer my questions.

I would also like to thank my kind teachers: Dr. Keith Furutani, Dr. Anita Berndt, Dr. Harry Johnson, Dr. Daniel Ricky, and Dr. Gabriel Thomas.

Thanks to my dear friend Conrad Yuen who helped me find my way to my PhD in Mcgill and for his kind help in editing several parts of this thesis.

I am grateful to all graduate students in Medical Physics department, Niranjan Venugopal, Peter Potrebko, Eric Van Uytven and Jim WJ for sharing their knowledge and experience with me.

Finally I thank my wife Marziyeh for her patience and support during my graduate studies.

Table of contents

1	Introduction	4
1.1	Purpose of radiation therapy:.....	4
1.2	Types of radiation therapy:.....	5
1.3	Rationale for treatment verification.....	6
1.4	Portal Imaging	8
1.4.1	Introduction.....	8
1.4.2	History.....	8
1.4.3	Electronic portal imaging devices.....	9
1.5	Image Registration.....	12
1.5.1	The need for an automated method.....	12
1.5.2	Interactive registration	13
1.5.3	Point-pair registration	14
1.5.4	Cross-correlation registration.....	15
1.5.5	Chamfer matching method.....	16
1.6	Image Registration for recovery of out-of-plane rotation	17
1.6.1	Registration methods based on anatomical landmarks	17
1.6.2	Registration methods based on artificial landmarks	19
1.7	Thesis overview	20
1.8	References	22
2	Fourier transform and Log-Polar conversion.....	26
2.1	Introduction	26
2.2	Fourier transform of an image and its basic properties	28

2.2.1	Introduction.....	28
2.2.2	Translation	30
2.2.3	Rotation:.....	32
2.2.4	Scaling.....	32
2.3	Fast Fourier Transform (FFT):	33
2.4	Log-polar conversion.....	35
2.5	References	38
3	Portal image registration for treatment verification	40
3.1	Introduction	40
3.2	Advantages of FFT based registration.....	41
3.3	Scale Signature	42
3.4	Rotation signature.....	51
3.5	Translation.....	54
3.6	References	59
4	Extraction of in-plane translation parameters	61
4.1	Reference and test images	61
4.2	Reducing sidelobe artifacts in the Fourier domain.....	65
4.3	Results for recovering of in-plane parameters.....	67
4.3.1	Scale recovery.....	67
4.3.2	Rotation recovery.....	71
4.3.3	Translation recovery	74
4.4	References	77
5	Recovery of out-of-plane rotation.....	78

5.1	Introduction	78
5.2	First approximation for image registration.....	80
5.2.1	Introduction.....	80
5.2.2	Mathematical properties of out-of-plane rotation	81
5.2.3	The results for first approximation	85
5.3	Second approach for image registration	89
5.3.1	Mathematical issues for the second approach.....	89
5.3.2	Approximations and results for second approach.....	95
5.4	Error analysis for recovery of out-of-plane rotation:.....	101
5.5	Discussion.....	105
5.6	References	110
6	Conclusion.....	112

1 Introduction

1.1 Purpose of radiation therapy:

The X-ray, a form of invisible high-energy radiation, was discovered by a German physicist, Wilhelm Roentgen. X-rays have been used to both diagnose and treat diseases. Images can be produced by allowing X-rays to penetrate an object. This is the basic principle for X-ray imaging of the body used in medical diagnostic purposes. It was later discovered that X-rays could kill cancerous cells and shrink tumors because of the high-energy emission. This method of treatment is called radiation therapy.

Radiation therapy uses X-rays, gamma rays and other sources of radiation to destroy cancer cells. Radiation kills cells by breaking up molecules and causing reactions that damage living cells. Sometimes the cells are destroyed immediately; sometimes certain components of cells, such as their deoxyribonucleic acid (DNA), are damaged, thereby affecting the ability to divide [1].

The radiation treatment is usually given using sophisticated equipment which produces a beam of high energy X-rays. The patient lies on a bed under the machine and the beam is directed at the site of the cancer. Modern equipment in radiation oncology is able to produce radiation beams of much greater energy, while maintaining a good spatial accuracy. Therefore, severe skin damage during treatment, which was common in the early days of radiation therapy treatment, is very rare with modern techniques.

Since emitted radiation energy does not distinguish between cancer cells and normal tissue, radiation fields are very carefully planned during the process of radiation treatment to protect normal tissue and vital organs of the patient. Certain predictable side

effects may occur after radiation treatment. The impact of side effects from radiation therapy is minimized using modern techniques.

The goal of radiation therapy can be curative. Radiation therapy is frequently used as adjuvant therapy to other treatments, most often with surgery and chemotherapy [2-4].

1.2 Types of radiation therapy:

There are two main types of radiation therapy: external beam radiation (Teletherapy) and internal radiation therapy (brachytherapy).

External Beam Radiation Therapy (Teletherapy): External beam radiation therapy is radiation delivered from an external source to the body and the radiation beam is directed at the tumor. Systems, which produce different types of radiation for external beam therapy, include orthovoltage X-ray machines, Cobalt-60 machines, linear accelerators, proton beam machines, and neutrons beam machines. A radiation oncologist makes decisions regarding the type of system that is best suited to treat a specific cancer patient. External beam therapy is the radiation therapy treatment option used for most cancer patients. It is used to treat many types of tumors including cancers of the head and neck area, breast, lung, rectum, and prostate.

Depending upon tumor location, different energies of radiation are used for external beam therapy. Low-energy radiation does not penetrate very deeply into the body and is used mainly to treat surface tumors such as skin cancer. High-energy radiation is used to treat other deeper cancers.

Most patients do not need to stay in the hospital while they are having external beam therapy. Many patients can go home following each treatment, and most patients can even continue with their normal daily activities.

Internal Radiation Therapy (Brachytherapy): Brachytherapy involves placing radiation sources as close as possible to the tumor site. Sometimes, they may be inserted directly into the tumor. The radioactive sources or isotopes are in the form of wires, seeds (or molds), or rods. This technique is particularly effective in treating cancers of the prostate, cervix, uterus, rectum, eye and certain head and neck cancers. It is also occasionally used to treat cancers of the breast, brain, skin, anus, esophagus, lung, and bladder. In some instances, brachytherapy may be used in conjunction with external beam therapy. When both forms are employed, the external beam radiation is intended to destroy cancerous cells in a large area surrounding the tumor, while the brachytherapy delivers a boost, or higher dose of radiation, to help destroy the main concentrated mass of tumor cells [2].

1.3 Rationale for treatment verification

To achieve the accurate delivery of a prescribed amount of radiation to a given volume of cancerous tissue within the patient while sparing normal healthy tissue, two basic criteria must be met. Firstly, the dose delivered by the treatment machine must be within the defined tolerance of the prescription. Secondly, the precise determination of the size and location of the tumor or target volume within the patient must be made.

There are several sources of error which can reduce the accuracy of radiotherapy: (i) incorrect alignment of the patient in the treatment beam, (ii) patient movement during

treatment, (iii) improper alignment of the shielding blocks, (iv) shifting of skin marks relative to internal anatomical structures and (v) mechanical alignment problems of the radiation treatment machine [3]. The result of these factors is to produce errors, known as localization errors, in which the localization of the cancerous tissue is misjudged, resulting in inadequate radiation treatment of the tumor and unnecessary exposure of normal tissue to radiation. The improved treatment of the cancer using current radiotherapy techniques can be achieved by ensuring accurate setup procedures and close verification of the treatment setup. Improved control of the treatment setup will allow for escalation of dose to the tumor and consequently, improved local control and in many cases, a higher cure rate [4].

To verify treatment set up, a pre-treatment simulation may be performed. The conventional simulation is performed by setting up the patient on a simulator machine under conditions that closely resemble the actual treatment. The simulator is equipped with an x-ray tube, which is used for taking x-ray radiographs. These radiographs show the prescribed size of the radiation field as well as the projection of the patient's anatomy along the direction of the prescribed beam, and are used for verifying patient setup during treatment. Alternatively patient positioning can be verified using digitally reconstructed radiographs (DRRs), which are generated within the treatment planning system using available 3-dimensional computed tomography data. Another method is portal imaging, which is a well-established method to verify the true position of radiation beam relative to the patient and will be discussed in detail in the next section.

1.4 Portal Imaging

1.4.1 Introduction

As mentioned earlier, radiation therapy requires careful verification of treatment delivery, since errors could have a crucial effect on the short and long term outcome of the treatment. To quantify deviations in patient setup and beam geometry during external beam radiotherapy, portal image devices and software tools for portal image analysis have been developed [5].

This review will examine some of the history of portal imaging and describe some of the devices (known as Electronic Portal Imaging Devices or EPID's) that are currently available commercially. We also discuss some practical considerations, examine some of the image processing image registration techniques that are necessary for portal imaging, and describe how these devices have been used clinically.

1.4.2 History

There is a long history of imaging with high-energy radiation beams. One of the first references to imaging in radiation therapy was by Nielsen and Jason who described a rotation therapy technique for treating cancer of the esophagus. In the treatment the therapeutic radiation exiting the patient hit the fluorescent screen which was viewed by an observer who was looking through a lead glass window. Not only did the observer view the treatment in real time, but corrections to the position of the beam were also made remotely during the treatment.

In 1960 Perryman et al described "Co-60 radiography". The technique used Kodak industrial film placed in the cassette where the standard intensifying screens had

been replaced by two 0.025cm lead sheets. The only drawback was that film development took approximately 30 minutes to complete. Finally in 1962, Spinger *et al* suggested an improvement to cobalt-60 radiography where two fluorescent screens were placed between the lead sheets and the film. This modification reduced the exposure time increased the contrast of the final radiographs.

About this time, non-film imaging methods started to be introduced into radiation therapy clinics. In 1958, a “television-roentgen system (TVR)” was described for monitoring the position of the patient during radiation therapy. The major limitation was that the TRV system had a small field of view. These efforts improved the quality of the images. However, the limited image quality and the need for contrast agents reduced the utilization of all imaging systems and they never came into widespread clinical use. As a result of the demand for more convenient methods of therapy verification has lead to development of modern Electronic Portal Imaging Devices (EPID’s) [6].

1.4.3 Electronic portal imaging devices

There is currently a great deal of interest in the use of electronic portal imaging devices for imaging of the patients prior to and during treatment. These images, obtained with a small fraction of the treatment dose, can be registered spatially with reference images to determine whether the patient is setup in the prescribed treatment position, then a correction can be applied before the remainder of the treatment dose is delivered [7].

Many different devices have been developed as an alternative to film. These devices can be divided into two categories: scanning systems using radiation detectors

that subtend only a small fraction of the radiation beam, scan underneath the patient to form the image and the area systems where the detector subtends the entire radiation beam. The following discussion concentrates on the matrix ion chamber and the TV camera-based system, which are both available commercially, as well as the amorphous silicon array.

The Matrix ion chamber: The matrix ion chamber device consists of two sets of electrodes that are oriented perpendicularly to each other separated by a gap, which is filled with a fluid that is ionized when the device is irradiated. Each set of electrodes consists of 256 electrodes. One set of the electrodes is connected to 256 electrometers and the other set of electrodes is connected to a high voltage supply, which can apply up to a 500 volt potential to each electrode individually. The matrix ion chamber array is read out by applying a high voltage to each of the high voltage electrodes in succession and measuring the signal generated in each of the 256 signal electrodes.

TV camera based EPID's: A TV camera based EPID uses a TV camera to view an x-ray detector through a 45° mirror (Figure 1.1). The x-ray detector consists of a metal plate and gadolinium oxysulfide (Gd_2O_2S) screen. When irradiated, high-energy electrons generated in the metal plate and Gd_2O_2S screen are converted into light. The video signal generated by this light is digitized and the digitized image can be viewed on the monitor located in the control area of the accelerator.

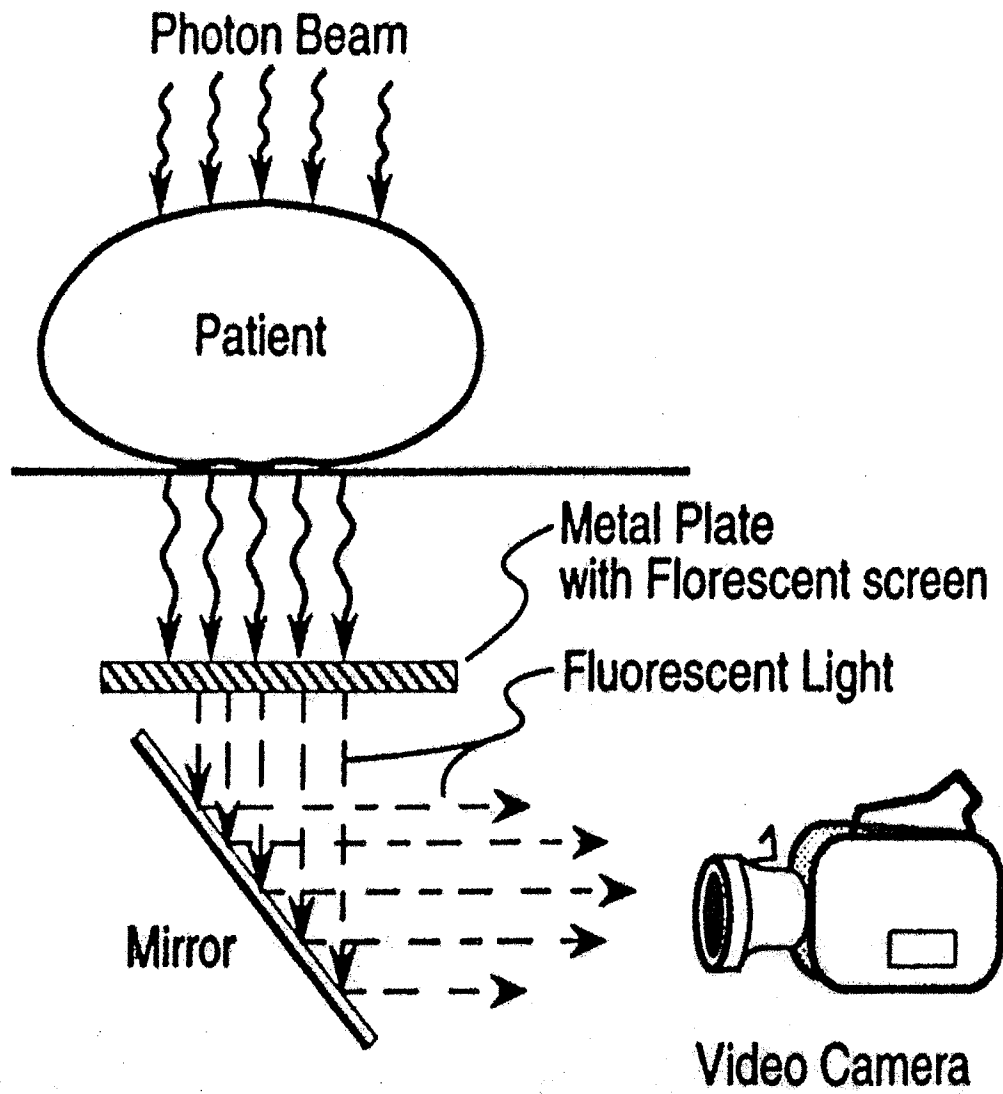


Figure 1.1 TV based portal imaging [2].

Flat panel EPIDs: One of the technological developments in megavoltage radiography is the development of the flat panel imaging devices, which consist of amorphous silicon arrays. Amorphous silicon arrays are large area integrated circuits fabricated from amorphous silicon, a material that exhibits extremely high resistance to radiation damage. The amorphous silicon consists of a two-dimensional matrix of thin transistors and photodiodes. These integrated circuits form a thin light sensor with a large area. The arrays have a high resistance to radiation damage, so they can be placed in direct contact with the metal plate phosphor screens that form the x-ray detector for EPID's. Much effort in developing amorphous silicon EPID's has been devoted to the development of readout electronics that can survive the radiation environment of the treatment room.

1.5 Image Registration

1.5.1 The need for an automated method

Portal images can be registered spatially with reference images to determine whether the patient is setup in the prescribed treatment position, with a possibility of a correction being applied before the remainder of the treatment dose is delivered [8]. The reference image can be a kilovoltage, megavoltage, or a digitally reconstructed radiograph. Sometimes the first approved portal image is also used as the reference image [9,10].

Developments in electronic portal imaging have led to a wide availability of commercial systems, but only a small fraction of the installed systems are actually being used clinically on routine and frequent basis. One of the major obstacles to widespread

clinical use of portal images is that with the large volume of portal image data and stringent time constraints, the conventional method by which the portal verification decision on the set up acceptability made by a qualified radiation oncologist is no longer sustainable. Visual comparison of the images is often complicated by the effect of the geometrical differences in the image forming process during simulation and during actual treatment. If we don't align the edges of the beam properly, corresponding features in both images may have a different position, orientation and magnification even when no treatment set up deviation is present. For these reasons, computerized methods using digital images are necessary for treatment verification, in particular if large numbers of portal images have to be analyzed in clinical practice. The three main capabilities required of such a tool are the automatic extraction of key features, the identification of differences between predicted and measured image, and making decisions and recommendations on the acceptability of a given treatment set-up [11-13].

Commonly, anatomical features have to be marked manually and are used when their shapes in the images do not change [9]. However, we may have an image distortion caused by noise, moving organs or a change of the patient projection angle due to shift and rotation of the patient. An intense research effort over the past several years has led to the development of a number of automated methods for field placement errors measurement [14-16].

1.5.2 Interactive registration

One of the intuitive ways of registering images is to use computer graphic techniques that allow users to overlay one image on top of another and to interactively,

translate, rotate, and scale the overlaid image until the anatomic features in both images coincide. Another method is to represent the anatomical information on the simulator image as a line drawing that can be superimposed over the portal image [10].

Alternatively, the two images can be displayed in a fashion that allows the anatomic features in both images to be visible at one time. Some of the techniques include using different colors to represent the gray scale values of each image. This method will then yield a third color, displaying the gray scale difference between the two images.

Despite the variety of displayed approaches, the line drawing technique is the method commonly used in commercially available EPIDs because line drawing does not obscure the structures in the portal images. However care must be taken when drawing the template, because studies have been shown that the largest registration inaccuracies are caused by inaccuracies in the template, not in registering the template with the anatomy in the portal image [6].

1.5.3 Point-pair registration

One of the frequently used methods to register image pairs of images is to identify the locations of common anatomical landmarks on the simulator and portal images. The coordinates of the points selected on the portal image can be transformed (i.e., translated, rotated, and scaled) until they best match the coordinates of the points on the simulator image. The best match is determined by the coordinate transform that minimizes the sum of squared distances between all of the corresponding point pairs. The sum of square

distances will be zero if all of the points selected on the portal image superimpose perfectly with those in the simulator images.

The accuracy of the point-pair registration technique depends on how well identical anatomical landmarks can be identified on each image and whether the landmarks have rigid positions with respect to each other. Because the point-pair registration assumes a rigid body transformation, distortion of the patient can produce an erroneous result. A number of studies have shown that the accuracy of the point pair registration technique depends on the treatment sites being evaluated and how widely spaced the points are in the image, but is independent of the number of the point pairs used for registration [6]. One of the difficult tasks is ensuring that identical anatomical landmarks have been selected on each image, otherwise the image registration will be inaccurate. Careful selection of the point pairs is however, time consuming.

1.5.4 Cross-correlation registration

The previous image registration technique requires the user to draw pair points. This requirement increases the workload and is an obstacle to routine use of the EPID technology in the clinic. As a result, efforts have been made to develop image registration techniques that can be semi or fully automated. One approach is to use cross correlation to identify identical anatomic landmarks on pair of images. In this approach the user identifies an anatomical landmark on the reference image by drawing a square or rectangular box around it (the reference window). A larger search region on the study image is identified (the search window) and the correlation coefficients are then calculated for every position of the reference window within the search window. The

maximum in the correlation coefficient identifies the location where the anatomical structure in the search window best matches those in the reference window. Once several anatomic landmarks have been identified by the cross correlation calculation, the paired points can be registered using the point pair registration technique.

The utility of cross correlation registration technique depends on several factors. Image quality must be good; otherwise anatomic structures of interest will be obscured by noise, thereby reducing the probability of identifying the identical structure. Most importantly, the cross correlation registration technique requires that gray scale values in the paired images be similar. Therefore the technique can only register a portal image with another portal image and not with another simulator image. Other image registration techniques must be used to generate a reference image before the cross correlation technique can be used. This reference is a portal image that has been translated, rotated and scaled so that the location of its anatomic structures is very similar to those in the simulator image. As a result, the cross correlation registration technique is not used widely, while studies have shown that it is a fast and convenient method of identifying positioning errors during radiation treatment.

1.5.5 Chamfer matching method

One of the more promising methods of portal image registration is known as Chamfer matching, which can register simulator and portal images automatically. Chamfer matching involves registering a drawing, generated from a simulator image, with what is known as a “cost function image”, generated from the portal image. The goodness of the fit between the drawing and cost function image is assessed by

determining the cost or penalty for the drawing being at a specific location with a specific orientation and scale with respect to the cost function image.

An important factor determining the accuracy of the chamfer matching registration technique is how well the features are extracted from the portal image. Using the images generated by the matrix ion chamber EPID, Gilhuijs and Van Herg showed that the accuracy of chamfer matching for translation is approximately 1.7mm [17]. However this registration technique fails for about 4% to 10% of images because it is unable to reliably extract the features from the portal images.

1.6 Image Registration for recovery of out-of-plane rotation

1.6.1 Registration methods based on anatomical landmarks.

Determining the three-dimensional translation and rotation of the patient can be performed by reconstruction of the three-dimensional positions of anatomical match points during the treatment session. This can be accomplished by combining the information in portal images obtained with orthogonal beams [24] or by performing a CT scan of the patient setup, using the treatment machine and the portal imaging device, prior to the actual treatment [25-27]. The underlying assumption is that the patient does not move during actual data acquisition.

A completely different method has been reported in which the patient setup for a lung field was reconstructed using a portal dose image which shows the transmitted radiation dose at every pixel. This dose image was compared with virtual dose images computed from different modifications of the CT data, simulating changes in the patient positioning and the amount and density of lung tissue per voxel. This method also

requires large computation times for repeated three-dimensional dose calculations, but yields the actual dose distribution to the patient directly [15].

An interesting work for 3-D verification of patient positioning was presented by J. Bijhold [7]. The method is based on the localization of match points in a single portal image, in a simulator image, and in CT-scan data. Anatomical points are selected that meet three constraints:

- (1) They can be identified and localized in three dimensions,
- (2) they are inside the radiation field, and
- (3) they have fixed positions relative to each other.

The solution for the displacement parameters is derived by solving the set of match equations. They provide two approaches based on two approximations [7]. In the first method, it is assumed that all anatomical match points are in one single plane perpendicular to the beam axis and that the distances between these points are small compared with the source to surface distance (SSD). The second method is referred to as a volume method, indicating that the points may be in a volume. This method assumes that all displacement parameters are small enough to allow for full linearization of the equations. In their work, there are two tables for detection of “displacement” in the presence of out-of plane rotation. The authors state that the differences between estimated and actual values for out-of-plane rotations were within 1° while uncertainty was estimated to be 0.3° [7]. There was no discussion regarding issues such as the range of the change in the out-of -plane rotation that was recovered.

1.6.2 Registration methods based on artificial landmarks

Several methods for determining the patient setup errors using radio-opaque markers affixed to the patient, instead of anatomical landmarks, have been proposed [28-31]. Images of radio-opaque markers have previously been used to register image sets, but their utility in automated detection of patient setup error has not been studied. The 3-D spatial location of the implanted markers (whether spherical or linear) is determined from two projections. Patient setup error, and hence movements required for patient realignment, can then be quantified by the 3-D spatial translation and rotation of the markers necessary to bring them back to the standard location. As the correction is known and can be completed in one step, numerous trials and errors to bring the patient to the desired position can be avoided. This is especially important when patient position is localized for every treatment, as the exposure from taking multiple repeat images could be significant.

Lam k. *et al* [28] have developed two algorithms to automate the process. The first algorithm is a general one, which locates the marker images on a pair of projection films and computes the 3-D location of the markers. It is used to determine the 3-D location of the markers of the first fraction of treatment. The second algorithm locates marker images on a pair of projection films by comparing them with a reference pair of projected films such as the pair obtained on the first fraction. It is used to determine the 3-D locations of the markers on subsequent fractions of treatment. As the projection films on the first fraction and subsequent fractions are very similar, even if there are setup differences, information on the reference films (such as shape, size, contrast, and

locations of marker images) can be exploited to facilitate the automatic detection of marker images. In their study, images of spherical radio-opaque markers affixed to a skull phantom were analyzed with computer algorithms. The effectiveness of using image-processing techniques to automatically locate the marker images is evaluated. There were four steps in the image processing: gray scale transformation, linear filtering, gray scale thresholding, and signal extraction. The precision in locating the markers in three dimensions is determined, and the accuracy of the system is used to estimate translations and rotations of the skull phantom, purposely misaligned from its nominal position. If the treatment fields include at least two fields from non-parallel directions, and all markers are within the treatment field, localization of the treatment field can be employed.

In their study, film is used to acquire the images. The film is processed and loaded to the film digitizer manually. This is a time consuming process, so this approach can not be used in on-line treatment verification or day to day treatment with a large number of patients.

1.7 Thesis overview

The Fourier transform is an important image processing tool in which each point represents a particular frequency contained in the spatial domain image. The Fourier transform is used in a wide range of applications, such as image analysis, filtering, reconstruction and image compression [18-23]. Morgan has used a technique to successfully align a pattern with a reference image. He has developed an algorithm for recovering transformation parameters from two images that differ by a Rotation-Scale-

Translation (RST). This process is useful in the alignment of an acquired image with a template for correlating a series of images, or the registration of separate bands of a composite image. This technique could be applied clinically to alignment of radiological and portal images [18].

Our approach for image registration in this study, which is based on the Fourier transform, extracts the magnitude of RST of a pattern portal image with respect to the reference image within a wide range of variation in RST. One problem inherent in current two-dimensional registration methods is related to the assumption that the anatomical structures to be registered lie in the same plane. So these methods cannot account for patient rotations out of the image plane.

The out-of-plane rotation results in an apparent distortion of anatomy between portal and reference images. The distortion can be mathematically predicted and is not the same for each dimension of the image. There is an image processing technique, which can be used for extracting the image characteristics in each dimension. In the second part of this work this method has been used to recover out-of-plane rotation using two-dimensional portal images.

1.8 References

1. H. Cember, *Introduction to health physics* (McGraw-Hill, 1996).
2. F. M. Khan, *The Physics of radiation therapy* (Williams and Wilkins, Baltimore, 1984).
3. A. Dutrix, "When and how can we improve precision in radiotherapy?" *Radiotherapy and oncology* **2**, 275-292 (1984).
4. H. Leszczynski, D. Provost, Bissett R, C. Cosby and S. Boyko, "Computer- assisted decision making in portal verification optimization of the neural network approach," *Int. J. Radiation Oncology Bio. Phys.* **45**, 215-225 (1999).
5. A. L. Fielding, P. M. Evans, D. Phil and C H Clark, "The use of electronic portal imaging to verify patient position during intensity-modulated radiotherapy delivered by the dynamic MLC technique," *Int. J. Radiation Oncology Bio. Phys.* **54**, 1225-1234 (2002).
6. P. Munro, "Portal imaging Technology , past present and future," *Seminars in Radiation Therapy* **5**, 115-133 (1995).
7. J. Bijhold, "Three-dimensional verification of patient placement during radiotherapy using portal images," *Med. Phys.* **20**, 347-356 (1993).
8. K. G. A. Gilhuijs, P. J. H. Van De Yan and M. Van Herk, "Automatic three-dimensional inspection of patient setup in radiation therapy using portal images, simulator images, and computed tomography data," *Med. Phys.* **23**, 389-399 (1996).
9. H. Meertens, J. Bijhold, J Strackee, "A method for measurement of field placement errors in portal images," *Phy. Med. Biol.* **35**, 299-323 (1990).

10. M. G. Herman, J.M. Balter J, D. A. Jaffray, K. P. McGee, P. Munro, S. Shlomo, M. Van Herk and J W Wong, "Clinical use of electronic portal imaging: Report of AAPM radiation therapy committee task group 58," *Med. Phys.* **28**, 712-737 (2001).
11. J. Bijhold, K. G. A. Gilhuijs, and M. Van Herk "Automatic verification of radiation field shape using digital portal image," *Med. Phy.* **19**, 1007-1014 (1992).
12. L. Dong and A. S. Tung, "Verification of radiosurgery target point alignment with an electronic portal image device (EPID)" *Med. Phys.* **24**, 263-267 (1997).
13. K. G. A. Gilhuijs, A. Touw, M. Van Herk and R. E. Vijlbrief "Optimization of automatic portal image analysis" *Med. Phys.* **22** 1089-1099 (1995).
14. J. Bijhold , J V. Lebesque, A. A. Hart and R. E. Vijbrief, " Maximizing setup accuracy using portal images as applied to a conformal boost technique for prostatic cancer." *Radiotherapy and oncology* **24**, 261-271 (1992).
15. J. Bijhold, M. Van Herk, R. Vijlbrief and J. V. Lebesque "Fast evaluation of patient set up during radiotherapy by aligning features in portal and simulator images," *Phy. Med. Biol.* **36**, 1665-1679 (1991).
16. D. S. Fritsch, E.L. Chaney, A. Boxwala, M. J. McAuliffe, S. Rajhavan Thall and J. R. D. Earnhart, "Core-based portal image registration for automatic radiotherapy treatment verification," *Int. J. Radiation Oncology Bio. Phys.* **33**, 1287-1300 (1995).
17. K. G. A. Gilhuijs , M van Herg, "Automatic online inspection of patient set up in radiation therapy using digital portal images." *Med phys.* **20** 667-677 (1993)

18. M. G. Morgan "An image registration technique for recovering rotation, scale and translation parameters." NEC Tech Report (1998)
19. P. Milanfar, "Two-dimensional matching filter," IEEE transaction on image processing **8**, 438-444(1999).
20. G. D. Borshuko, G Bozdagi , Y. Altunbasa and M. Tekalp. "Motion segmentation by multistage affined classification," IEEE transactions on image processing **6**, 1591-1594 (1997).
21. S. Alliney, "Digital analysis of rotated images," IEEE transactions on pattern analysis and machine intelligence, **15**, 499-504 (1993).
22. E. De Castro and C. Morandi "Registration of Translated and rotated images using finite Fourier transform," IEEE transactions on pattern analysis and machine intelligence **9**, 700-703 (1987).
23. B. S. Reddy and B. N. Chatterji, "An FFT-based technique for translation, rotation, and scale invariant image registration," IEEE transactions on image processing **5**, 1266-1271 (1996).
24. A. F. Thornton, Jr., R. K. Ten Haken, A. Gerhardsson, and A. Correl, "Three-dimensional motion analysis of an improved head immobilization system for simulation, CT, MRI, and PET imaging," Radiother. **20**, 224-228 (1991).
25. A. E. Lujan, J. M. Balter, R. K. Tenhaken "Determination of rotations in three dimensions using two dimensional portal imaging," Med. Phys. **20**, 703-708 (1998)

26. J. Lattanzi, S. McNeely, A Hanlon, I Das, Schulthies TE, L Hanks " Daily CT localization for correcting portal errors in the treatment of prostate cancer," *Int. J. Radiat. Oncol. Biol. Phys.* **5** 1070-1086 (1998)
27. H. Guan, Yin FF, Y. Zhu, J H Kim "Adaptive portal CT reconstruction: a simulation study," *Med. Phys.* **10**, 2014- 1152 (2000).
28. K. L. L. Lam, R. K. Ten Haken, D. L. McShan. and A. F. Thomson, Jr, "Automated determination of patient setup errors in radiation therapy field using spherical radio-opaque markers," *Med. Phys.* **20**, 1145- 1152 (1991).
29. E. Grusell, A. Montelius, K. R. Russell, E. Blomquist, L. Pellettieri, A.using Lilja, U. Mostrom, and P. Jakobsson, "Patient positioning for fractionated precision radiation treatment of targets in the head using fiducial markers" *Radiother. Oncol.* **33**, 68-72, (1994).
30. L. E. Millendar, M. Aubin, J. Pounliot, K. Shinohara, M. Roach "Daily electronic portal imaging for morbidly obese men undergoing radiotherapy for localized prostate cancer," *Int. J. Radiat. Oncol. Biol. Phys.* **1**, 6-10 (2004)
31. R. S. Katee, M. J. Olofsen, M. B.Verstraate, S. Quint, B. J. Heijmen "Detection of organ movement in cervix cancer patients using a fluoroscopic electronic portal imaging device and radio opaque markers," *Int. J. Radiat. Oncol. Biol. Phys.* **2**, 522-531 (2002)

2 Fourier transform and Log-Polar conversion

2.1 Introduction

The Fourier transform is an important image processing tool in which each point represents a particular frequency contained in the spatial domain image. The Fourier transform is used in a wide range of applications, such as image analysis, filtering, reconstruction and image compression [1-6].

The Fourier transform, $F(u)$, of a single variable, continuous function, $f(x)$, is defined by this equation:

$$F(u) = \int_{-\infty}^{+\infty} f(x)e^{-j2\pi ux} dx \quad (2.1)$$

where $j = \sqrt{-1}$. Conversely, from $F(u)$, one can obtain $f(x)$ by means of the inverse Fourier transform

$$f(x) = \int_{-\infty}^{+\infty} F(u)e^{j2\pi ux} du \quad (2.2)$$

These two equations comprise the Fourier transform pair. They indicate that a function can be recovered from its transform. These equations are easily extended to two variables,

$$F(u, v) = \int_{-\infty}^{+\infty} \int_{-\infty}^{+\infty} f(x, y)e^{-j2\pi(ux+vy)} dx dy \quad (2.3)$$

In general, we see from Eq. 2.3 that the components of Fourier transform are complex quantities. In the analysis of the complex numbers, it is often convenient to express $F(u)$ in polar coordinates:

$$F(u) = |F(u)|e^{-j\varphi(u)} \quad (2.4)$$

where

$$|F(u)| = [R^2(u) + I^2(u)]^{1/2} \quad (2.5)$$

$|F(u)|$ is called the *magnitude* or *spectrum* of the Fourier transform, and

$$\varphi(u) = \tan^{-1} \left[\frac{I(u)}{R(u)} \right] \quad (2.6)$$

$\varphi(u)$ is called the *phase angle* or *phase spectrum* of the transform. In Eq. 2.5 and 2.6, $R(u)$ and $I(u)$ are the real and imaginary parts of $F(u)$ respectively. Image enhancement is dependent primarily with properties of the spectrum. Another quantity that is used later in this chapter is the power spectrum, defined as the square of the Fourier transform:

$$P(u) = |F(u)|^2 = R^2(u) + I^2(u) \quad (2.7)$$

The term spectral density is also used to refer the power spectrum.

2.2 Fourier transform of an image and its basic properties

2.2.1 Introduction

A gray scale image can be represented by a two dimensional matrix where the magnitude of each element is related to the brightness of related point in the image. The discrete Fourier transform (DFT) of an image $f(x,y)$ of size $M \times N$ is given by the equation

$$F(u,v) = \frac{1}{MN} \sum_{x=0}^{M-1} \sum_{y=0}^{N-1} f(x,y) e^{-j2\pi(ux/M+vy/N)} \quad (2.8)$$

The frequency domain is the space defined by values of the Fourier transform and its frequency variables (u,v) . The Fourier spectrum, phase angle and power spectrum for a function with two variables are defined as:

$$|F(u,v)| = [R^2(x,y) + I^2(x,y)]^{1/2} \quad (2.9)$$

$$\varphi(u,v) = \tan^{-1} \left[\frac{I(u,v)}{R(u,v)} \right] \quad (2.10)$$

and

$$P(u,v) = |F(u,v)|^2 = R^2(u,v) + I^2(u,v) \quad (2.11)$$

For an image $f(x,y)$ the value of the Fourier transform at the origin is equal to the average gray level of the image. If $f(x,y)$ is real, its Fourier transform is conjugate symmetric, that is :

$$F(u, v) = F^* (-u, -v) \quad (2.12)$$

where “ * ” indicates the standard conjugate operation on a complex number.

From this it follows that

$$|F(u, v)| = |F(-u, -v)| \quad (2.13)$$

which illustrates that the spectrum of the Fourier transform is symmetric.

Eq. 2.8 shows that each term of $F(u,v)$ contains all values of $f(x,y)$, modified by the values of the exponential terms. Thus, with the exception of trivial cases, it is usually impossible to make direct associations between specific components of an image and its transform. However some general statements can be made about the relationship between the frequency component of Fourier transform and spatial characteristics of an image. For instance, since frequency is directly related to the rate of change, it is not difficult to intuitively associate frequencies in Fourier transform with patterns of intensity variation in an image. As mentioned before, the slowest varying frequency component ($u=v=0$) corresponds to the average gray level of an image. As we move away from origin of the Fourier transform, the low frequencies correspond to the slowly varying components of the image. As we move further away from the origin the higher frequencies begin to correspond to faster and faster gray level changes in the image. These are the edges of

objects and other components of an image characterized by abrupt changes in gray level, such as noise [7].

In Figure 2.1(a), a white rectangle is superimposed on a black background. The Fourier Transform of this image is shown in Figure 2.1(b). In Figure 2.1(b) the separation of spectrum zeros in the horizontal direction is twice the separation of zeros in the vertical direction. In this figure the effects of the rotating and scaling in the Fourier transform of an image are illustrated.

2.2.2 Translation

Let f_1 and f_2 be two images that differ by a displacement (x_0, y_0) :

$$f_2(x,y)=f_1(x-x_0,y-y_0) \quad (2.14)$$

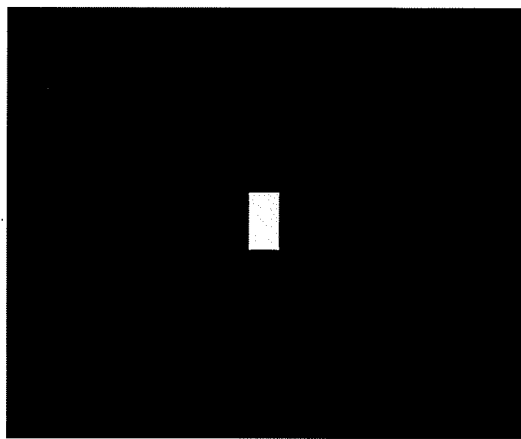
For their corresponding Fourier transforms, F_1 and F_2 are related by

$$F_2(u,v)=F_1(u,v) e^{-i2\pi(ux_0+vy_0)} \quad (2.15)$$

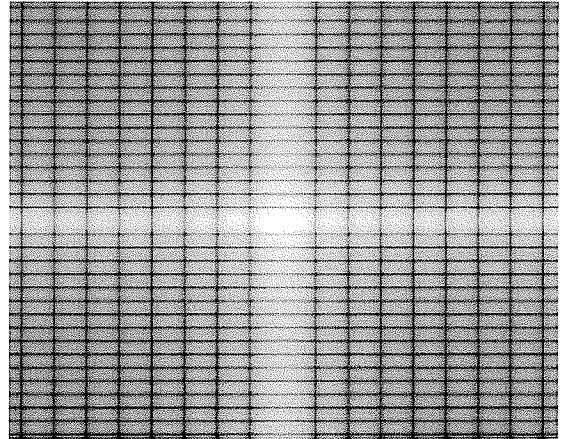
Taking the magnitude of Fourier transforms we have:

$$|F_2(u,v)| = |F_1(u,v)| \quad (2.16)$$

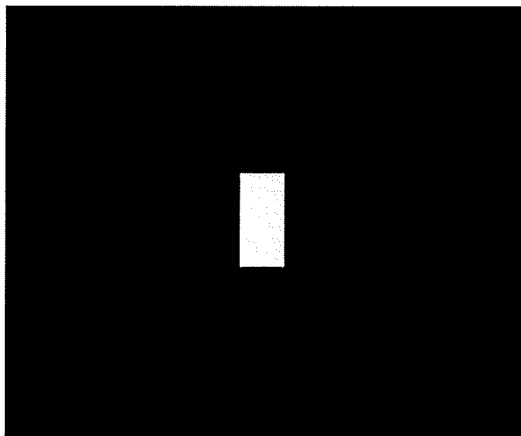
so the translation only changes the phase of the Fourier transform and has no effect on the magnitude of the Fourier transform.



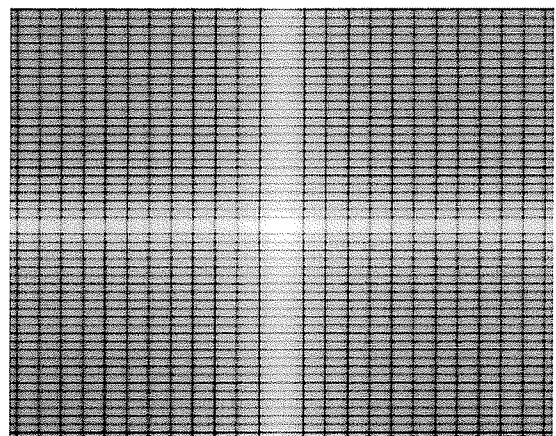
(a)



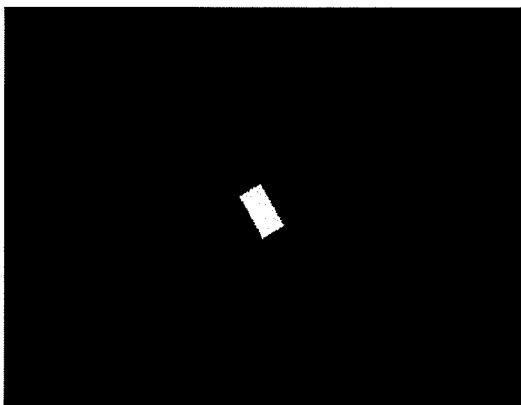
(b)



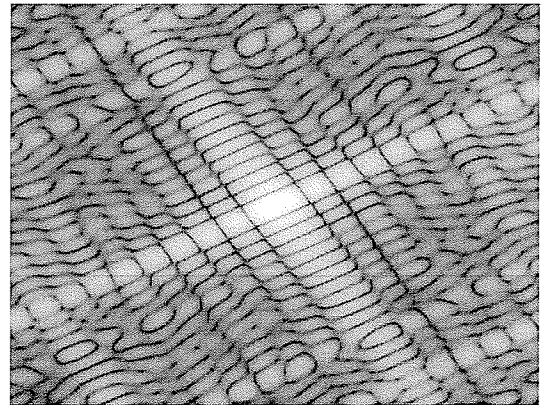
(c)



(d)



(e)



(f)

Figure 2.1. A white rectangle (a) as a test image and its Fourier Transform (b). The scaled (c) and rotated (e) replica of the test image and their Fourier transforms (d) and (f) respectively.

2.2.3 Rotation:

If image f_1 is rotated through an angle of θ_0 , to create an image f_2 , the Fourier transform of the images in the polar domain are given by [11]:

$$F_2(\rho, \theta) = F_1(\rho, \theta - \theta_0) \quad (2.17)$$

Where $\rho = \sqrt{u^2 + v^2}$.

One sees that F_2 is equal to a replica of F_1 rotated through angle $-\theta_0$. We can see this fact in Figure 2.1. Therefore if an image is rotated through a particular angle θ_0 , the Fourier transform of the image will rotate by $-\theta_0$.

2.2.4 Scaling

If f_2 is a scaled image of f_1 with scale factor of s , for the Fourier transforms we have:

$$F_1(u, v) = \frac{1}{s^2} F_2(u/s, v/s) \quad (2.18)$$

Therefore scaling an image by a factor of $1/s$ is equivalent to scaling the Fourier transform by s and multiplying the magnitude of the Fourier transform by $1/s^2$.

Figure 2.1 (c) and (e) are the scaled and rotated replica of Figure 2.1(a). We can see the effect of the scaling and rotation on the Fourier transform in Figure 2.1(d) and (f) respectively.

2.3 Fast Fourier Transform (FFT):

In the equation 2.8, if we consider the function f as a one-dimensional function with N elements, it is quite complicated to solve as it involves many additions and multiplications involving complex numbers on the order of N^2 . With $N=8$ it would require 49 complex multiplications and 56 complex additions to work out the discrete Fourier transform (DFT). At this level it is still manageable, however a realistic function could have $N=1024$ elements which requires approximately 10^6 complex multiplications and additions. The number of calculations required soon mounts up to unmanageable proportions (Figure 2.2). The FFT accomplishes the same task on the order of $N \log_2 N$ operations. For $N=1024$, FFT methods will require approximately 10^4 operations. This is a computational advantage of 100 to 1. If, for instance, $N=8192(2^{13})$, the computational advantage grows to 600 to 1.

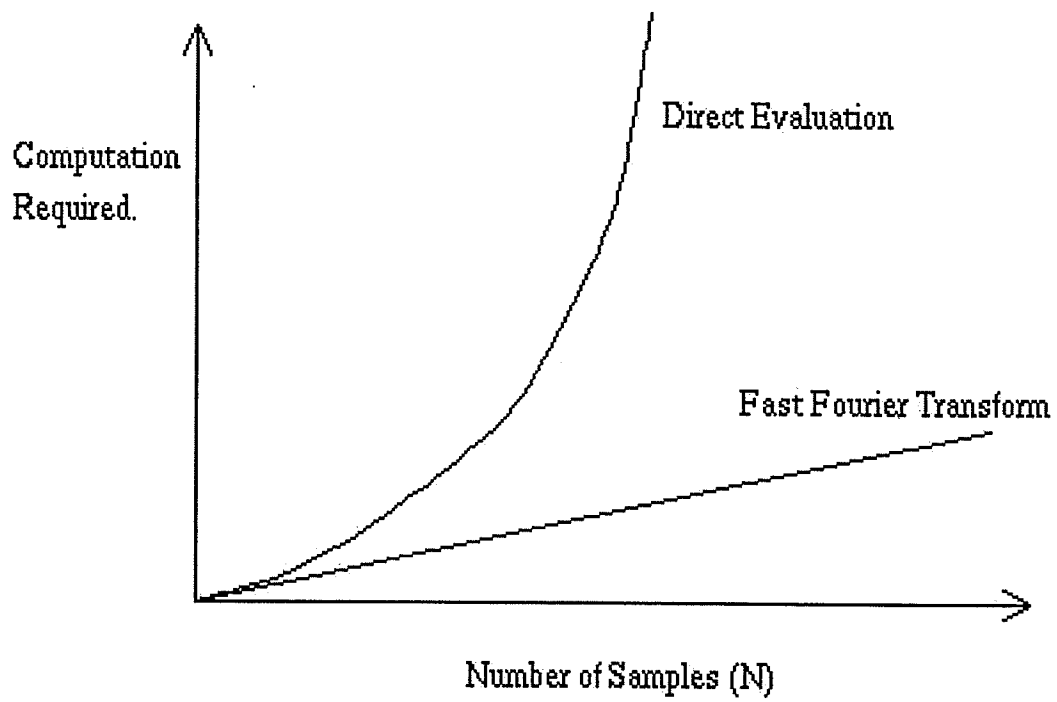


Figure 2-2 Comparison between computation number of direct evaluation of the Fourier transform and Fast Fourier Transform.

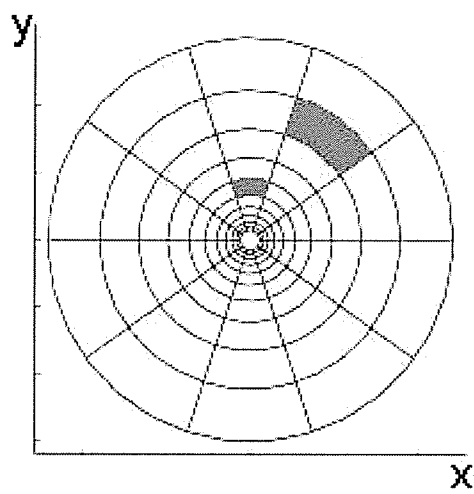
2.4 Log-polar conversion

The log-polar image geometry was first motivated by its resemblance with the structure of the retina of some biological vision systems and by its data compression qualities. When compared to the usual Cartesian images, the log-polar images allow faster sampling rates on artificial vision systems without reducing the size of the field of view and the resolution on the central part of the retina (fovea). Recently it has been noticed that the log-polar geometry and log-polar transform also provides important algorithmic benefits. This transform is a well-known space-variant image-encoding scheme used in some computer vision systems [7-10]. The log-polar mapping has the advantage of selective image data reduction, but also has some mathematical invariance properties (i.e. scaling and rotation) which are especially useful for image processing, in particular for moving objects.

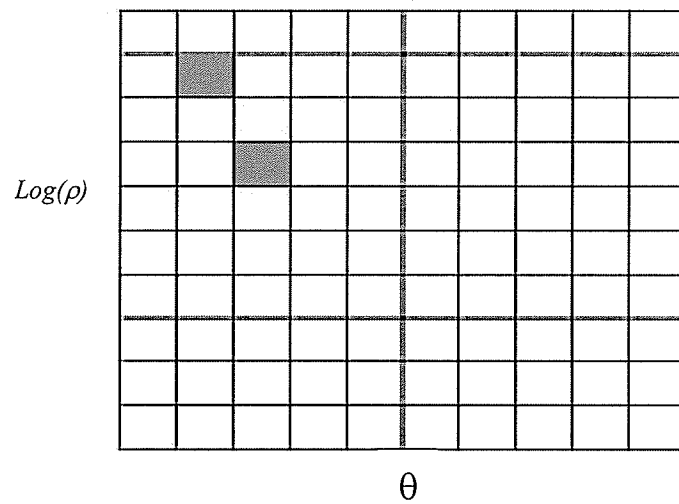
The log-polar transformation is a conformal mapping from the points on the Cartesian image $I(x,y)$, Figure 2.3(a) and (c), to points in the cylinder log-polar plane $I_L(\log\rho, \theta)$ Figure 2.3(b) and 2.3(d). The mapping is described by these equations:

$$\rho = \sqrt{[(x - x_0)^2 + (y - y_0)^2]} \quad (2.20)$$

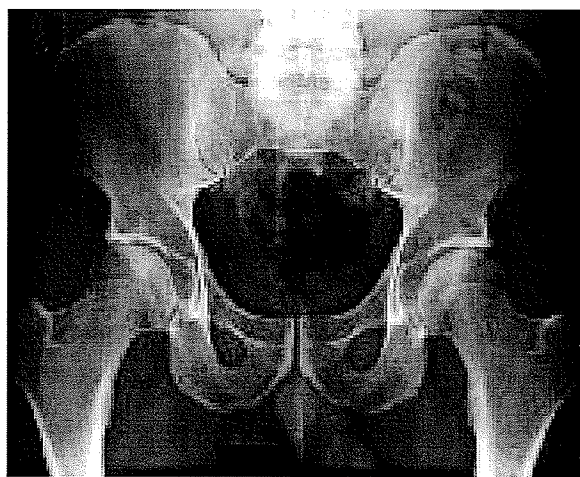
$$\theta = \tan^{-1} \left[\frac{y - y_0}{x - x_0} \right] \quad (2.21)$$



(a)



(b)



(c)



(d)

Figure 2.3. The transformation of original image in Cartesian scale (a) to log-polar scale (b). Image (c) is a x-ray pelvis in Cartesian scale, which after mapping to log-polar scale is transferred to image (d). In image (d) we see the resolution is decreased in the higher rows for larger ρ . These are the parts with a larger distance from the origin in image (c).

In the log-polar transform, the center is located at the specific point, (x_0, y_0) , called the transform origin. The $\log(\rho)$ -coordinate of a point in I_L is proportional to the logarithm of the radial distance from the origin of the corresponding point in I . The θ coordinate is equal to angular distance of the corresponding point from the x-axis in I . In digital images, the mapping from I to I_L is discrete and not one to one. The inverse mapping of the pixels of I_L partitions I into a set of regions resembling a cobweb (Figure 1(a)). The area of the regions increases with radial distances from the origin of I and in the region of I sufficiently far from the origin the mapping from I to I_L is many pixels to one. Figure 2.3(d) illustrates that image resolution decreases with axial distance from the origin in the Cartesian image.

2.5 References

1. M. G. Morgan "An image registration technique for recovering rotation, scale and translation parameters." NEC Tech Report (1998).
2. P. Milanfar, "Two-dimensional matching filter," IEEE transaction on image processing 8 , 438-444(1999).
3. G. D Borshuko, G Bozdagi , Y. Altunbasa and M. Tekalp. "Motion segmentation by multistage affined classification," IEEE transactions on image processing 6, 1591-1594 (1997).
4. S. Alliney, "Digital analysis of rotated images," IEEE transactions on pattern analysis and machine intelligence 15, 499-504 (1993).
5. E. De Castro and C. Morandi "Registration of Translated and rotated images using finite Fourier transform," IEEE transactions on pattern analysis and machine intelligence 9, 700-703 (1987).
6. B. S. Reddy and B. N. Chatterji, "An FFT-based technique for translation, rotation, and scale invariant image registration," IEEE transactions on image processing 5, 1266-1271 (1996).
7. R. C. Gonzales, R. E. Woods, *Digital Image Processing* (Addison- Wesley, 1992).
8. M. Tistarelli and G. Sandini, "On the advantage of polar mapping for direct estimation of time-to-impact from optical flow," IEEE transactions on pattern analysis and machine intelligence 15, 401-410 (1993).
9. G. Wolberg, S. Zokai, "Robust image registration using Log-polar transform," Proc.of IEEE Intl. Conf. on image processing, 2000

10. C. Y. Lin, M. Wu, J. A. Bloom, I. J. Cox, M. A. Miller and Y. M. Lui, "Rotation, scale and translation resilient watermarking for images," *IEEE transactions on image processing* **10**, 767-782 (2001).

3 Portal image registration for treatment verification

3.1 Introduction

Registration algorithms attempt to align a portal image over a reference image so those features present in both images are in the same location. This process is useful in the alignment of an acquired image over a template, a time series of the same scene, or a separate band of a composite image (coregistration). One practical application of this process is the alignment of portal images during treatment.

In this chapter the registration technique for portal images is presented which is based on the method that Morgan has used for image registration [1]. In this technique the properties of FFT in log polar domain have been used. These properties have also been shown using sample images. This image is an X-ray pelvis image with the well-defined borders (Figure 3-1).

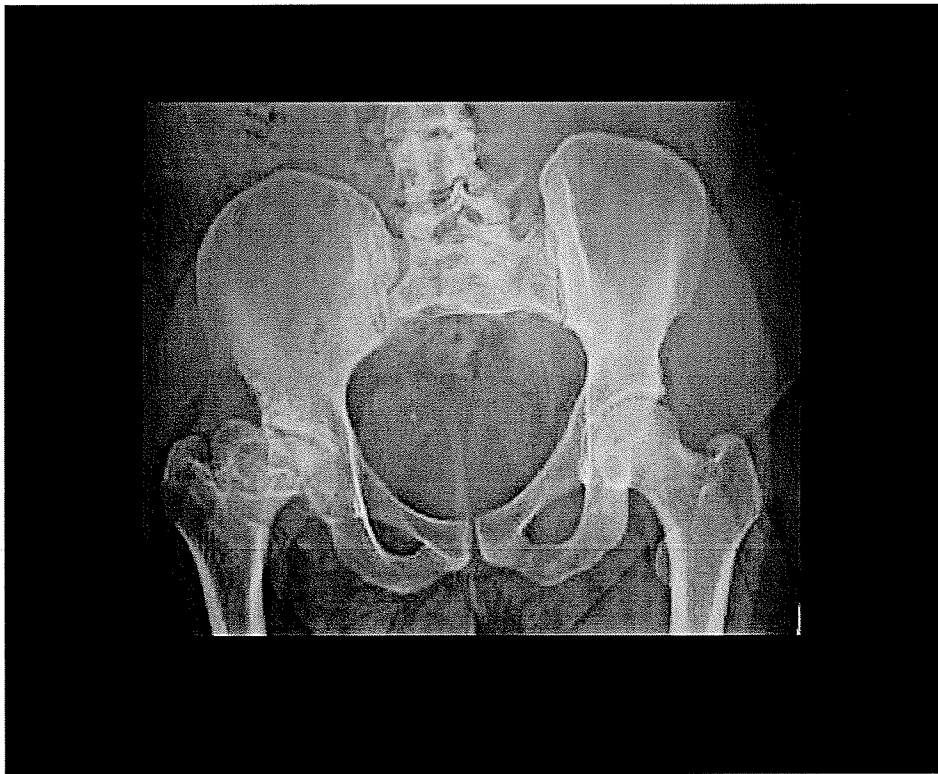


Figure 3.1 An X-ray image of the pelvis, which is used for the illustration of the registration steps.

The image in Figure 3.1 has better contrast than portal images and it is used only for illustration of different steps of the image registration technique. The results of the image registration are also illustrated for this image to show the abilities of this registration technique using a good contrast image.

3.2 Advantages of FFT based registration

In previous portal imaging work, as discussed in section 1.5, the edges of the elements are used for image registration, which in the frequency domain means that only the high frequency part of the image is considered for image registration [2-10]. The advantage of using the Fourier transform approach is that a wide range of frequencies are employed for image registration and intrinsically contains more information [11]. So, with this approach, in the case of image distortion or even if some parts of the original image go outside of the borders the Rotation-Scale-Translation (RST) parameters, can still be extracted. Another advantage of this approach is that this technique is automatic and needs no visual comparison between the pattern and reference images.

The FFT based technique for image registration is presented in a paper by Morgan [1]. Morgan presents an algorithm for recovering transformation parameters from two images that differ by a Rotation-Scale-Translation (RST) transformation in the presence of noise and occlusion from alignment. Any RST transformation may be expressed as a combination of a single translation, single rotation, and single scale factor all operating in the plane of the image. He expresses such a transformation as a pixel-mapping function that maps a reference image into a pattern image.

In Chapter 2 it was illustrated that rotating an image in the pixel domain by angle θ is equivalent to rotating the magnitude of its Fourier transform by $-\theta$. Expanding an image in the pixel domain by a scale factor of s is equivalent to scaling of the Fourier transform by $1/s$ and multiplying the height (amplitude) of the magnitude of the Fourier transform by $1/s^2$. Translation in the pixel domain has no effect on the magnitude of the Fourier transform. This enables us to recover the parameters of rotation and scale through separate operations on the magnitude of the Fourier transform.

Our registration technique operates in three phases, one for each transformation parameter: scale, rotation, and the translation vector. The scale and rotation phases are independent and may be performed in parallel. The translation phase can proceed only after the rotation and scales are known. The following discussion describes how to use transformations and correlations to recover the transformation parameters. All of the programs are written with MATLAB.

3.3 Scale Signature

A clinical image may have rotation, scaling and translation simultaneously. The purpose of the scale signature is to recover the scale factor in the presence of the rotation and translation. The digital portal image is mapped into a translation and rotation invariant space that changes with scale factor. For a discrete case the scale signature is resistant to translational and rotational change and can be used to effectively recover the scale factor [1].

The scale signature of the image $f(x,y)$ is derived by:

- 1) Calculating the Fourier transform of the image:

$$F_1(u,v) = FT(f(x,y)) \quad (3.1)$$

2) Taking the magnitude of the resultant Fourier transform of the image.

$$F_2(u,v) = |F_1(u,v)| \quad (3.2)$$

3) Converting the magnitude of the Fourier transform to log-polar space.

$$F_3(\log\rho, \theta) = \text{log-polar}(F_2(u,v)) \quad (3.3)$$

4) Integrating along the θ axis and dividing by the radius (which produces a one-dimensional function)

$$S(\log\rho) = \frac{1}{\rho} \int_0^{\pi} F_3(\log\rho, \theta) d\theta \quad (3.4)$$

This function is called the “scale signature” of the image and is invariant to image rotation. Section 2.2.2 illustrates that the magnitude of the Fourier transform is independent of the translation. By integrating over angle, and dividing by radius, the effect of the rotation is eliminated and the resulting function only depends on the scale factor. The Fourier transform of the real image has a 180° rotational symmetry, so the integration bounds can be reduced by a factor of 2. For digital images, the continuous function, S , in Eq. 3.4 is a discrete function so summation with respect to θ is made over “interpolated” points in log-polar space.

Let $f_2(x,y)$ be the scaled replica of $f_1(x,y)$ with the scale factor s , using Eq. 2.18 we have

$$F_1(u,v) = \frac{1}{s^2} F_2(u/s, v/s) \quad (3.5)$$

Converting the magnitude of the Fourier transform of the images to log-polar space gives:

$$\rho_1 = \sqrt{u^2 + v^2}$$

$$\theta_1 = \tan^{-1}\left(\frac{u}{v}\right)$$

$$\rho_2 = \sqrt{\left(\frac{u}{s}\right)^2 + \left(\frac{v}{s}\right)^2}$$

$$= \frac{1}{s} \sqrt{u^2 + v^2} = \frac{\rho_1}{s} \quad (3.6)$$

$$\theta_2 = \tan^{-1}\left(\frac{u/s}{v/s}\right)$$

$$= \tan^{-1}\left(\frac{u}{v}\right) = \theta_1 \quad (3.7)$$

So in Eq. 3.5, the Fourier transform magnitude of two images in log-polar space is related by

$$F_1(\log \rho, \theta) = \frac{1}{s^2} F_2\left(\log \frac{\rho}{s}, \theta\right) \quad (3.8)$$

And finally for the scale signature of two images we have:

$$S_1(\log \rho) = S_2\left(\log \frac{\rho}{s}\right)$$

$$= \frac{1}{s^2} S_2(\log \rho - \log s, \theta) \quad (3.9)$$

Therefore the scale signature, S , has the property that scaling an image by a factor of s is equivalent to translation of S by $-\log s$. Scaling by a factor of s for any translation and rotation transformation in the pixel domain is equivalent to shift in the S domain by $-\log s$, and the normalized one dimensional correlation between the scale signatures of two images will be unity (maximum) at $-\log s$. This means that after calculating the scale signature of the images, a simple one-dimensional correlation can be used to recover the scale parameter. For the sample image, shown in Figure 3.1, the different steps for extracting the scale signature and resulting correlation will be shown.

Figure 3.2 shows the magnitude of Fourier transform of the image. Figure 3.3 show the magnitude of the Fourier transform in log polar domain. The transformation is done using equations 2.20 and 2.21. For log polar conversion the origin is placed in the center of the image. The horizontal axis is 360 pixels equal to one rotation with one-degree steps and the vertical axis is related to the radial distances from the origin in 500 increments, which are log spaced. In Figure 3.3 the decreasing of the resolution is decreased for larger radial distances.



Figure.3.2 Magnitude of Fourier transform of the X-ray pelvis image

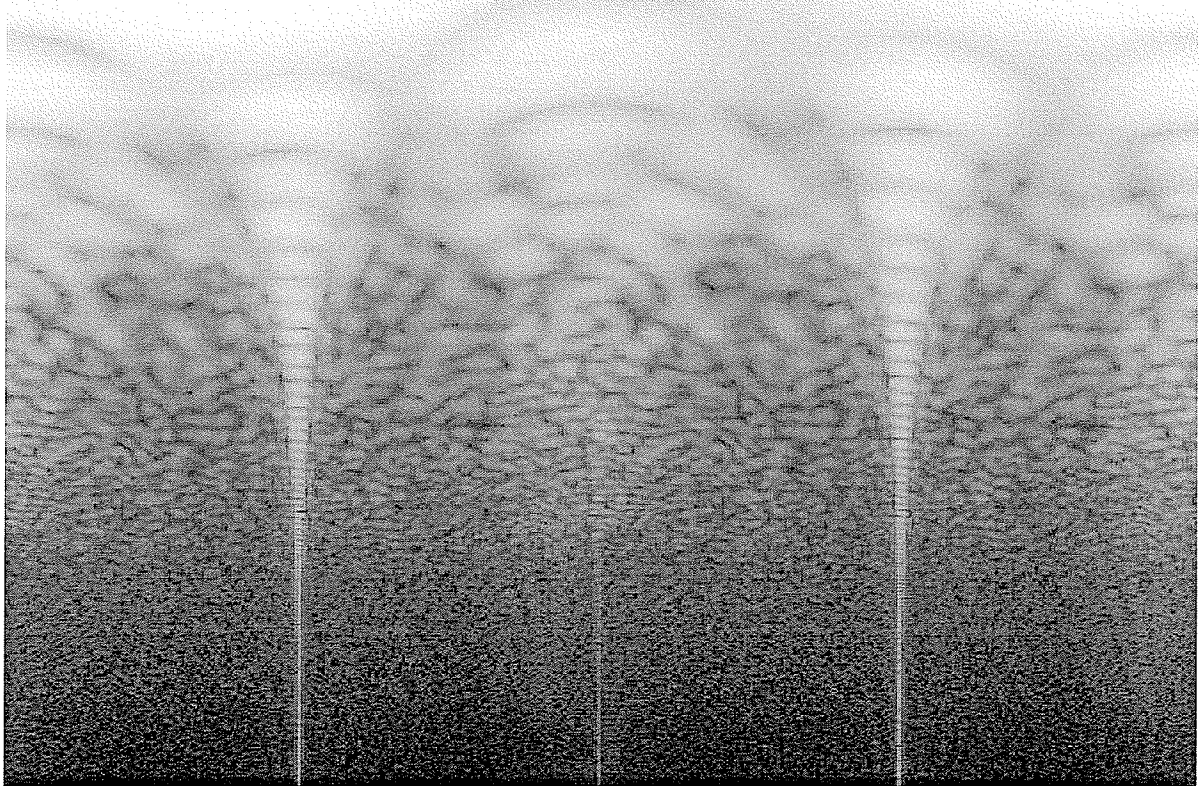


Figure 3.3 Magnitude of Fourier transform in Log-polar domain

There is an important technical point for log polar conversion in digital images as a discrete function. The current points in Cartesian domain are converted to log polar domain. However these points are not necessarily located in the coordinates needed to get a log polar image. In order to obtain the values for log polar domain, a linear “interpolation“ between the existing values was performed.

a log polar image. In order to obtain the values for log polar domain, a linear “interpolation” between the existing values was performed.

In the next step, Eq. 3.4 is used to create the scale signature of the image. To see the effect of the scale factor several images were created with different scale factors between 0.4 and 2.0. This is accomplished using “imresize” function in MATLAB. Figure 3.4 shows the scale signature of these images. As we see there is a clear shift in the scale signature of images.

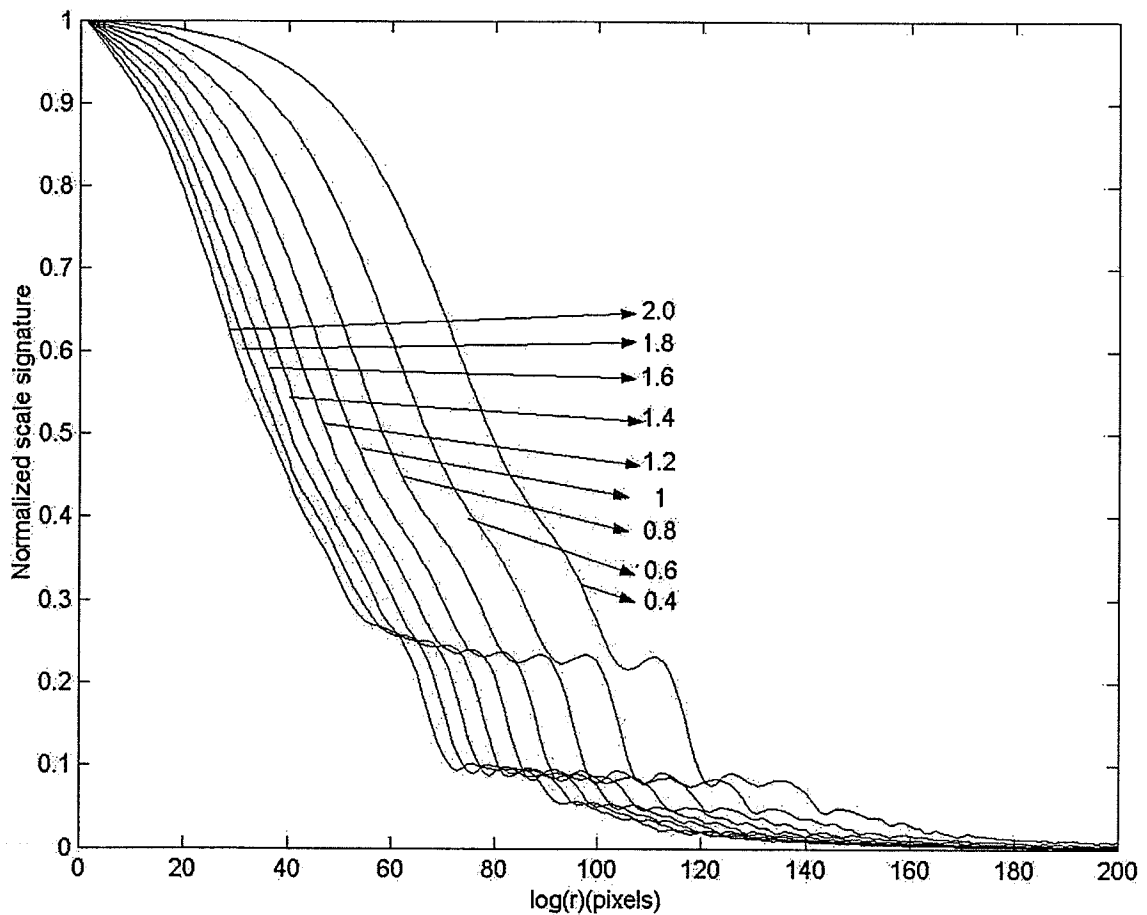


Figure 3.4 The normalized scale signatures for images with scale factor between 0.4 and 2

After calculating the scale signature of the images, the scale signature of the reference image (in this case the image with scale factor of 1) should be correlated with scale signature of the other images. Figure 3.5 shows the results of this correlation. There is a shift in the peaks for the different scale factors. The goal is to illustrate the relation of the shift with respect to the scale factor. According to Eq3.9 the shift is the function of $-\log(s)$. The Figure 3.6 illustrates the negative of the shift of the peaks with respect to different scales. The log of the original scale factors, which is the ideal result, also has been plotted in this figure to compare with the results. In this figure, there is a clear log shaped function of the shift versus the scale factor and this enables us to recover the scale factor.

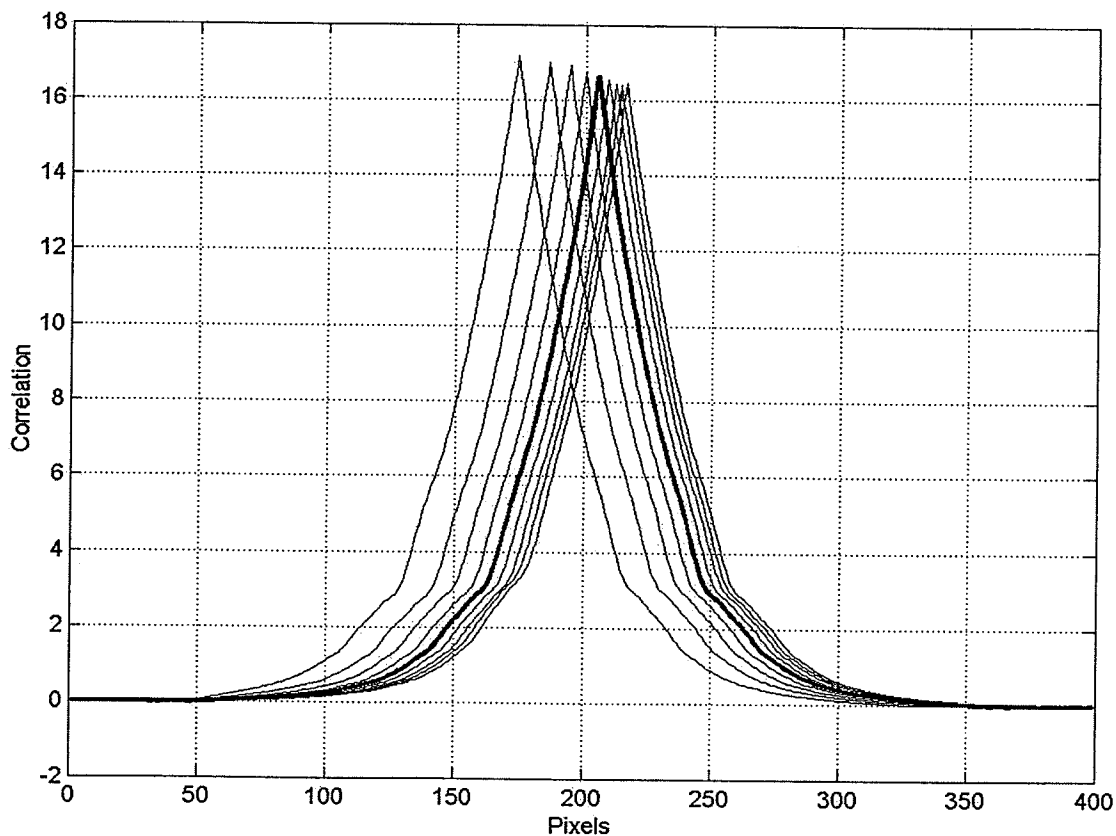


Figure 3.5 The correlation of the scale signature of the reference image (scale=1) with other images (with scales factor between 0.4 and 2). The correlation of the reference image with itself is shown with a thicker line.

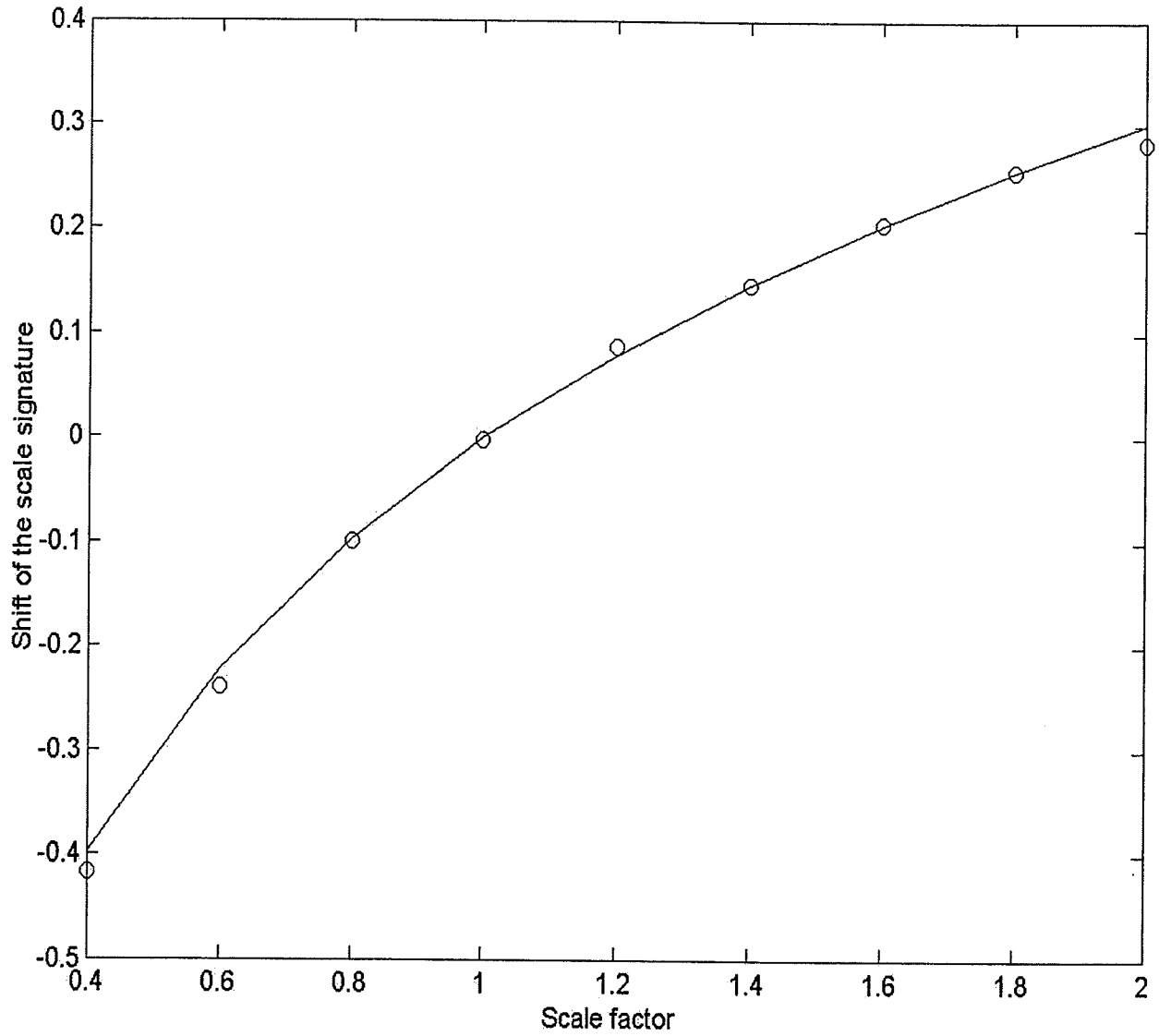


Figure 3.6 Shift of the scale signature of the images with scale factors between 0.4 and 2 with respect to the scale signature of the reference image (circles). Log of the scale factors also has been plotted (solid line) to compare with the results.

3.4 Rotation signature

In this section we discuss how we recover the rotation parameter, θ , which is the rotation of one image with respect to another in the presence of scaling and translation. For a discrete image the rotation signature is independent of translation and scaling of the original image, although an overall change in the magnitude may occur [1]. To this end we follow a similar approach as we did to calculate the scale signature, from steps 1 to 3 in section 3.3. The rotation signature is defined by integrating the magnitude of the Fourier transform of the image in log-polar space, $(F_3(\log\rho,\theta), \text{Eq. 3.3})$ over the ρ axis. This integration produces a one-dimensional function, which is the rotation signature:

$$R(\theta) = \int F_3(\log\rho, \theta) d\rho \quad (3.10)$$

A rotation by angle θ in the image domain corresponds to a shift of $-\theta$ in the R domain. If image f_2 is rotated with respect to f_1 with an angle of θ_0 and its corresponding magnitudes of Fourier transform in the log-polar domain are F_1 and F_2 , then:

$$F_2(\log\rho, \theta) = F_1(\log\rho, \theta - \theta_0) \quad (3.11)$$

and

$$R_2(\theta) = R_1(\theta - \theta_0) \quad (3.12)$$

The normalized circular correlation of the two scale signatures has a maximum value of unity at $-\theta$.

To illustrate the rotation signature and the effect of a rotation on the rotation signature, 9 images are created from x-ray images of the pelvis. These images are rotated with respect to the original image with an angle ranging from -20 to 20 with 5-degree steps. One of these images with a 30° rotation is shown in Figure 3.7. The rotation signature of these images is shown in Figure 3.8. The regular shift in the rotation signature, which is correspond to 5-degree steps in rotation is illustrated.



Figure 3.7 Rotated replica of the x-ray image with angle of 30°

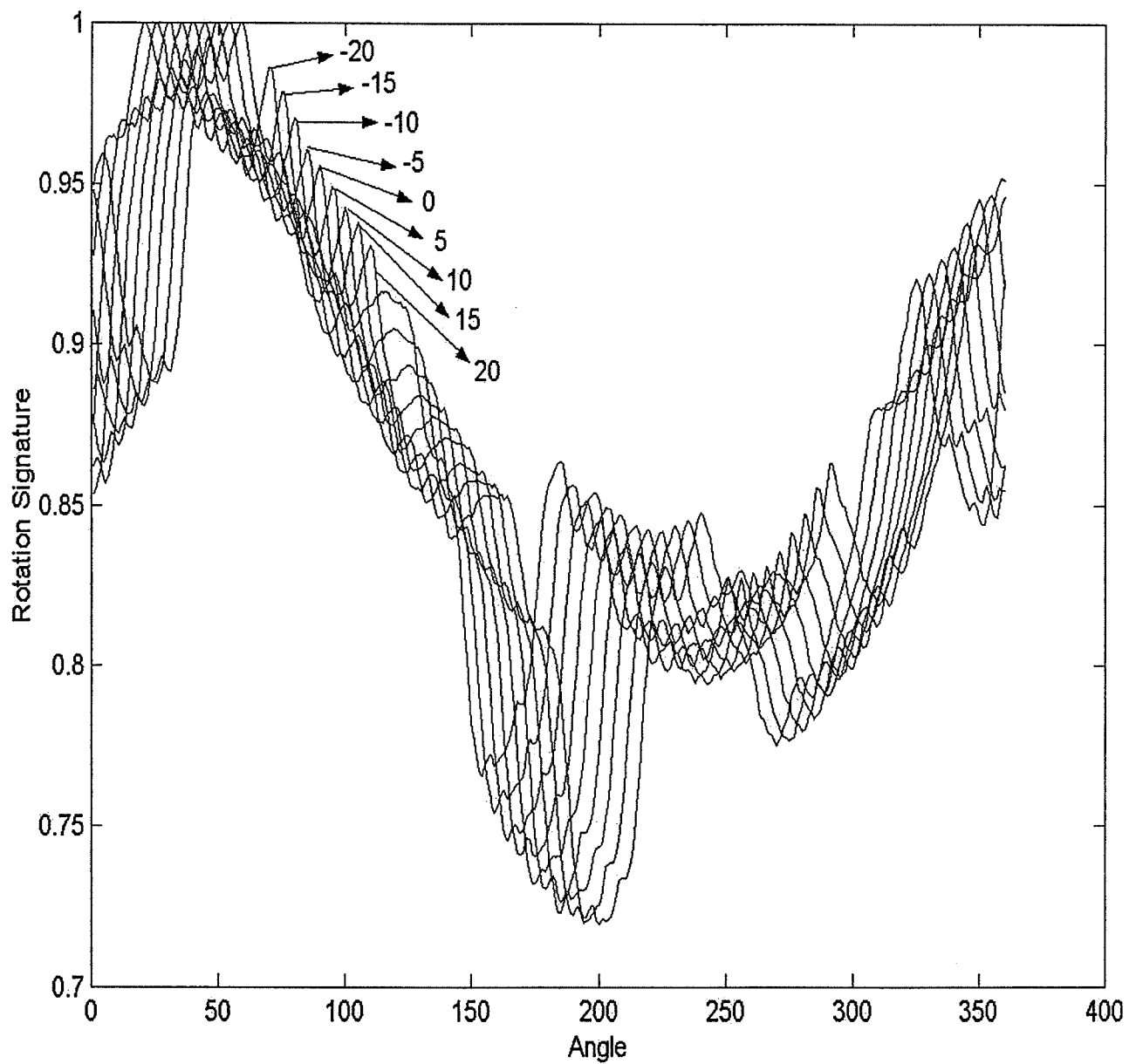


Figure 3.8 Normalized rotation signature of the images with different angles with respect to the original image. The angle is between -20 to 20 with 5 -degree steps.

3.5 Translation

Extracting the translation parameters is done after recovering the scale and rotation factors. If the scaling and rotation factors of the pattern image with respect to the original image are represented by s and θ , the pattern image is re-scaled by magnitude of $1/s$ and it is rotated by $-\theta$. As a result there are now two images where the only difference is a translation of the images.

The phase correlation technique is used for recovering the translation parameters in such an image [12-17]. The phase correlation technique provides a measure of similarity between two discrete images and relies on the translation properties of the Fourier transform, as shown in Eq. 2.15. This technique is an important tool in the broadcasting domain for a wide range of applications including motion measurement for noise reduction, archive restoration, and video compression. It is insensitive to change in the brightness and noise [12].

Phase correlation is based on the evaluation of the phase of the Cross Power Spectrum. The "phase correlation formula" is given by:

$$\frac{F_1(u, v) \cdot F_2^*(u, v)}{|F_1(u, v) \cdot F_2^*(u, v)|} = e^{i2\pi(ux_0 + vy_0)} \quad (3.13)$$

F_1 and F_2 are the Fourier transforms of the two images that only differ by displacement. The “*” means the complex conjugate of the function. The left side of the equation is the normalized Cross Power Spectrum of the image and in the right side the magnitude of

the translation along the x and y direction is x_0 and y_0 respectively. The inverse Fourier transform of this equation theoretically has an impulse. This impulse in the X, Y plane is located at (x_0, y_0) . A typical phase correlation is illustrated in Figure 3.9.

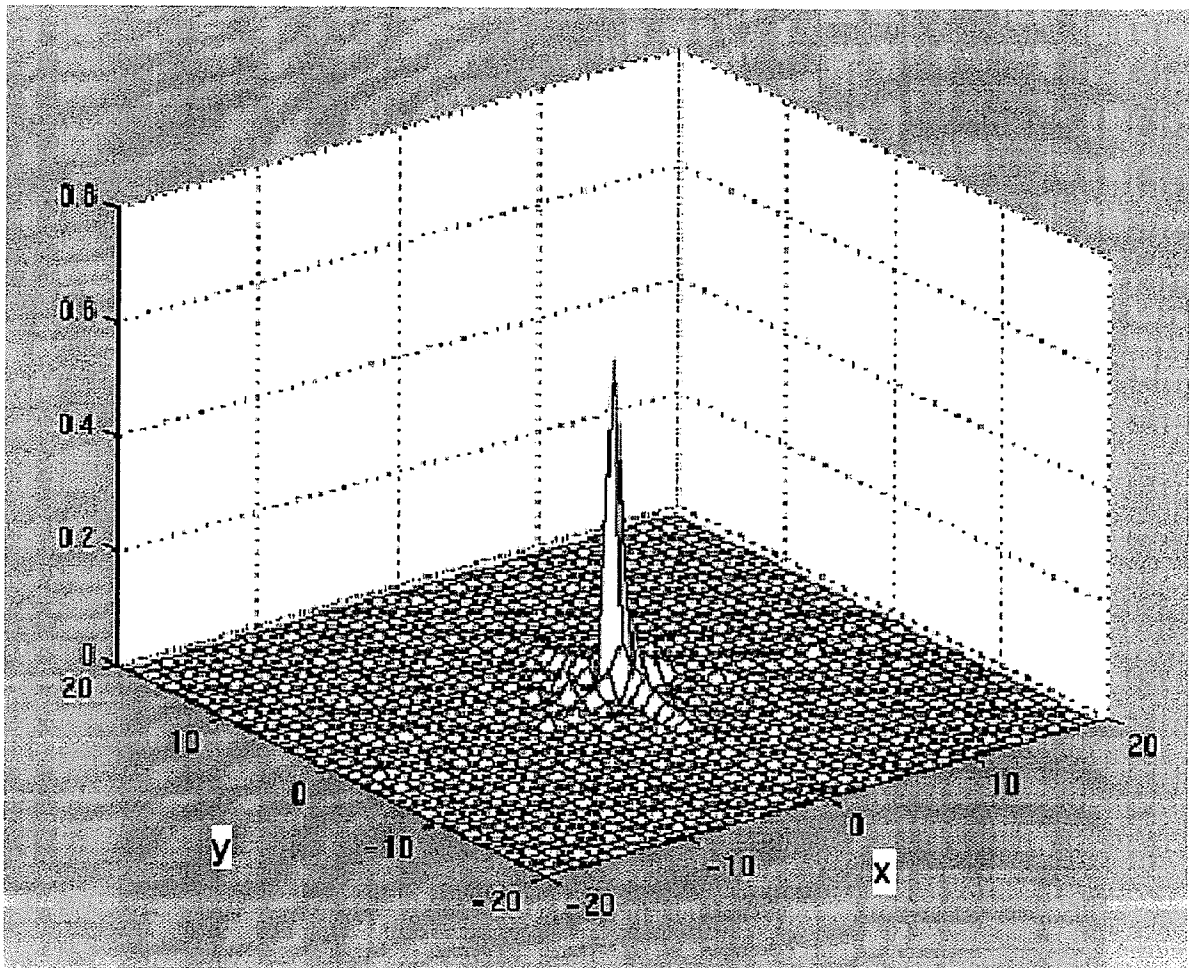


Figure 3.9 A typical Phase Correlation surface

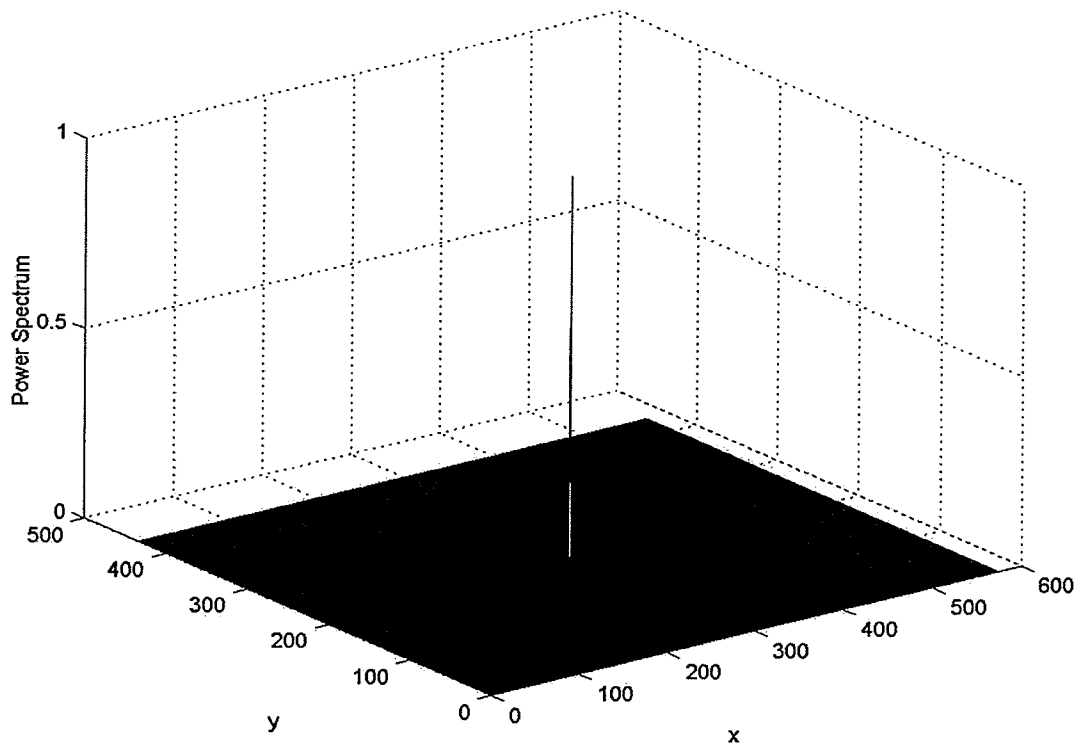
For two images in the presence of rotation, scaling, and translation, the translation parameters can be determined using the following steps:

- 1) Extracting the rotation and magnification parameters.
- 2) Correction for the rotation and magnification.
- 3) Taking the Fourier transform of the corrected images.
- 4) Calculating the phase correlation formula.
- 5) Taking inverse Fourier transform of the phase correlation.
- 6) Determining the location of the impulse, which is located in translation parameters (x_0, y_0) .

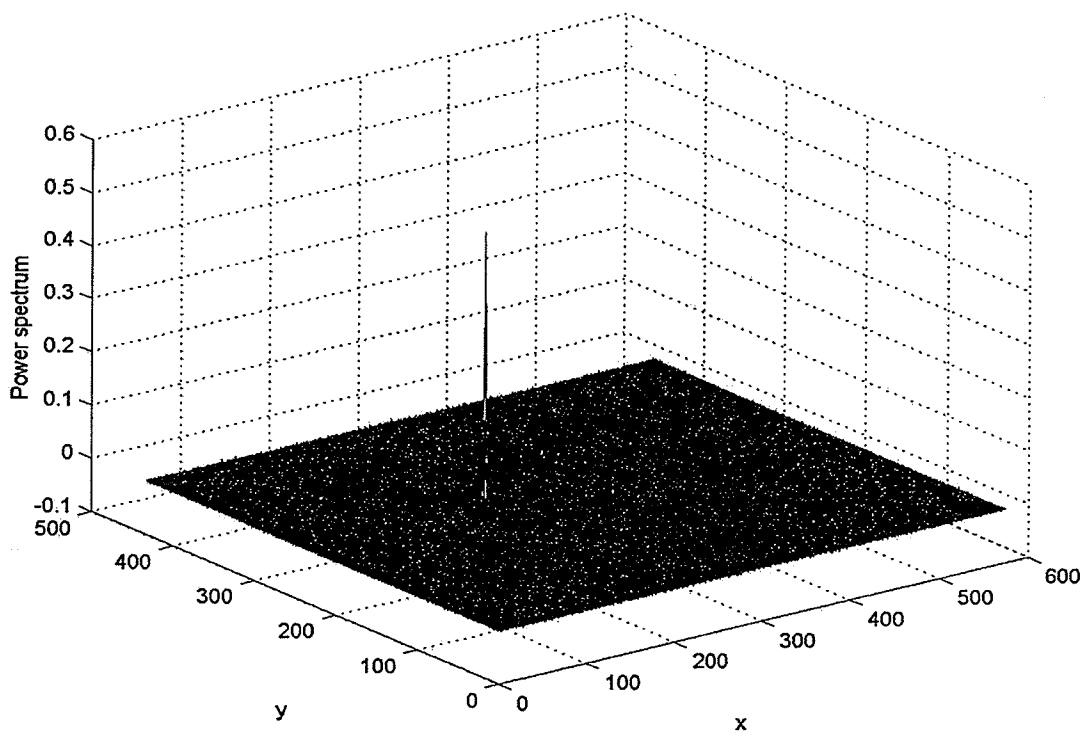
For identical images, without the rotation and scaling, the result has a unique peak. In Figure 3.10 the pelvis image is translated with respect to Figure 3.1. The phase correlation of Figure 3.1 with itself and Figure 3-10 are shown in Figure 3.11(a) and (b) respectively. The position of the peak in (b) is shifted with respect to position of the peak in (a).



Figure 3-10 Translated replica of the x-ray pelvis image in Figure 3.1



(a)



(b)

Figure 3-11 Normalized power spectrum of the figure 3 1 with itself (a) and figure 3 1 with figure 3-11

3.6 References

1. M. G. Morgan, "An image registration technique for recovering rotation, scale and translation parameters," NEC Tech Report, Feb (1998)
2. J. Bijhold, "Three-dimensional verification of patient placement during radiotherapy using portal images," *Med. Phys.* **20**, 347-356 (1993)
3. H. Meertens, J. Bijhold, J Strackee, "A method for measurement of field placement errors in portal images," *Phy. Med. Biol.* **35**, 299-323 (1990).
4. J. Bijhold, K. G. A. Gilhuijs, and M. Van Herk "Automatic verification of radiation field shape using digital portal image," *Med. Phys.* **19**, 1007-1014 (1992).
5. L. Dong and A. S. Tung, "Verification of radiosurgery target point alignment with an electronic portal image device (EPID)" *Med. Phys.* **24**, 263-267 (1997).
6. K. G. A. Gilhuijs, P. J. H. Van De Yan and M. Van Herk, "Automatic three-dimensional inspection of patient setup in radiation therapy using portal images, simulator images, and computed tomography data," *Med. Phys.* **23**, 389-399 (1996).
7. J. Bijhold , J V. Lebesque, A. A. Hart and R. E. Vijlbrief, " Maximizing setup accuracy using portal images as applied to a conformal boost technique for prostatic cancer." *Radiotherapy and oncology* **24**, 261-271 (1992).
8. J. Bijhold, M. Van Herk, R. Vijlbrief and J. V. Lebesque "Fast evaluation of patient set up during radiotherapy by aligning features in portal and simulator images," *Phy. Med. Biol.* **36**, 1665-1679 (1991).

9. D. S. Fritsch, E.L. Chaney, A. Boxwala, M. J. McAuliffe, S. Rajhavan Thall and J. R. D. Earnhart, "Core-based portal image registration for automatic radiotherapy treatment verification," *Int. J. Radiation Oncology Bio. Phys.* **33**, 1287-1300 (1995).
10. K. G. A. Gilhuigs , M van Herg, "Automatic online inspection of patient set up in radiation therapy using digital portal images." *Med Phys.* **20** 667-677 (1993).
11. R. C. Gonzales , R. E.Woods, *Digital Image Processing* (Addison- Wesley, 1992).
12. H. Foroosh, B. Z. Zerubia and M. Berthod, "Extension of phase correlation to subpixel registration," *IEEE transactions on image processing* **11**, 188-200 (2002).
13. D. E. Castro and C. Morandi "Registration of translated and rotated images using finite Fourier transform," *IEEE Trans. on pattern analysis and machine intelligence* **5**, 700-703 (1987).
14. J. J. Pearson, D.C. Hines, S. Golosman and C. D. Kaglin, " Video rate image correlation processor," *Proc IEEE* **54**, 947-955 (1966).
15. L. Hill and T. Vlachos, "On the Estimation of Global Motion using Phase Correlation for Broadcast Applications," *IEEE International Conference on Image Processing and it's Applications (IPA 99)*, 721-725 (1999).
16. L. Hill and T. Vlachos, "Shape Adaptive Phase Correlation", *IEEE Electronics Letters*, **37**, 1512-1513 (2000).
17. C. Kuglin and D. Hines, "The Phase Correlation Image Alignment Method," *Proc. of the IEEE Int. Con. on Cybernetics and Society*, 163-165 (1975)

4 Extraction of in-plane translation parameters

4.1 Reference and test images

In this chapter the technique discussed in chapter 3 for comparing a pattern image with a reference image is implemented for a clinical image. The algorithms for image registration are written using MATLAB software. The algorithms were tested using a digitally reconstructed radiograph of the pelvis as a reference image. The reference image, which has a resolution of 384x512 pixels, is shown in Figure 4.1(a). This image is an anterior-posterior view of the pelvis and the contrast of the image is poor with respect to x-ray images. From this reference, a set of test images was created with known RST parameters, a sample of which is shown in Figure 4.1(b). This image is a replica of the Figure 4.1(a) with scale factor of 1.2, rotation of 15° , and translation of 12 and 8 pixels in x and y directions respectively. In order to create the test images, functions from the “image processing toolbox” of MATLAB were used. These functions will be discussed later in this section.

As the scale factor increases, some parts of the image exceed the size of the frame, placing an upper limit on the scale parameter, which can be recovered by any algorithm [1]. For clinically generated portal images there are also constraints to the magnification of the image. For Linac mounted EPIDs, the distance between the source and portal imaging device is constant and magnification depends on the placement of the patient with respect to the source and detector [2-3].

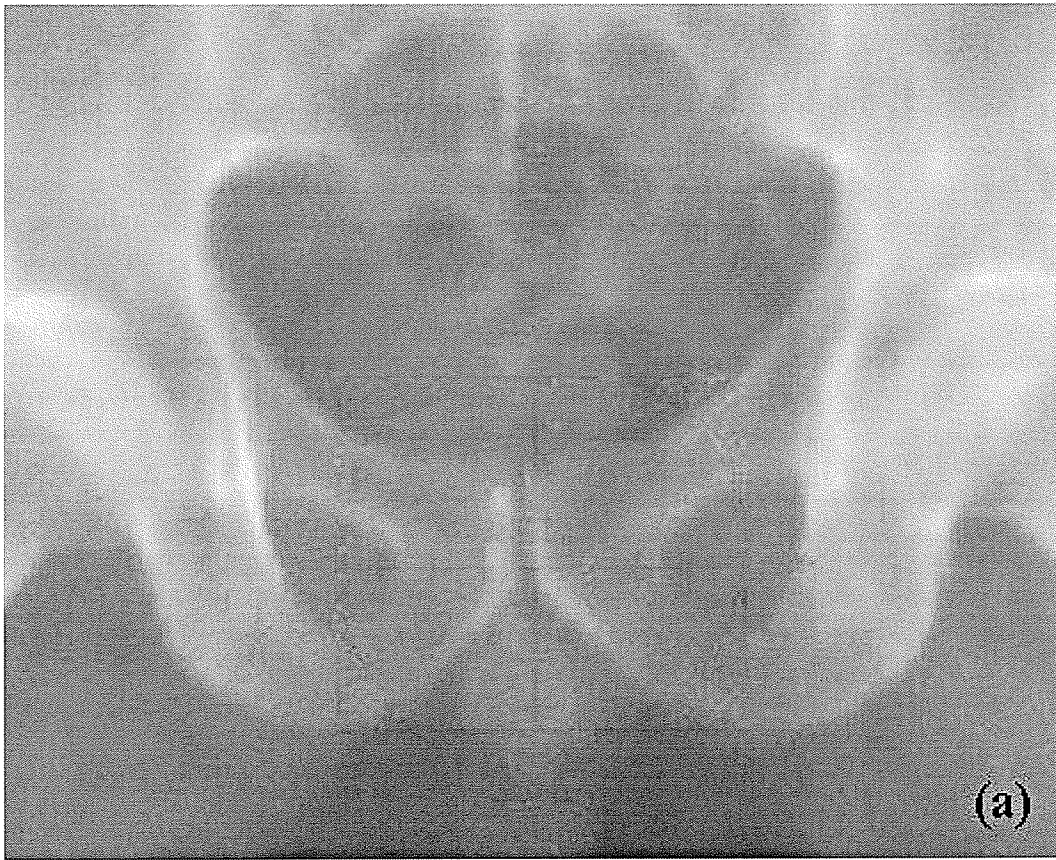


Figure 4.1. Reference image and one of the test images. a) A digitally reconstructed radiograph of a pelvis as a reference image. b) The image of the same pelvis as a test image, which is scaled, rotated and translated with respect to the reference image.

An example of deviation in treatment set up is shown in Figure 4.2. In this set up the prescribed source to surface distance, SSD, is assumed to be 100cm.

The wrong SSD in this example is 80cm. To calculate the magnification due to this wrong set up we have:

$$\frac{d1}{H} = \frac{x}{SSD1} \rightarrow d1 = \frac{xH}{SSD1} \quad (4.1)$$

$$\frac{d2}{H} = \frac{x}{SSD2} \rightarrow d2 = \frac{xH}{SSD2} \quad (4.2)$$

$$\frac{d2}{d1} = \frac{xH}{SSD2} \frac{SSD1}{xH} \rightarrow \frac{d2}{d1} = \frac{SSD1}{SSD2} \quad (4.3)$$

$$\frac{d2}{d1} = \frac{100}{80} = 1.25 = 125\% \quad (4.4)$$

With a similar calculation it can be shown that for the wrong SSD of 120 cm the scale factor is 0.83. Assuming the set up errors of ± 20 cm for the prescribed 100cm SSD, the scale factor changes from 0.83 to 1.25. The test images were created with 7 scales ranging between 0.86 and 1.28, corresponding to ± 20 cm error in SSD. For each scale factor a group of images was created with rotations, between 0° and 45° in 5-degree steps. Translation parameters are varied over a range of ± 40 pixels.

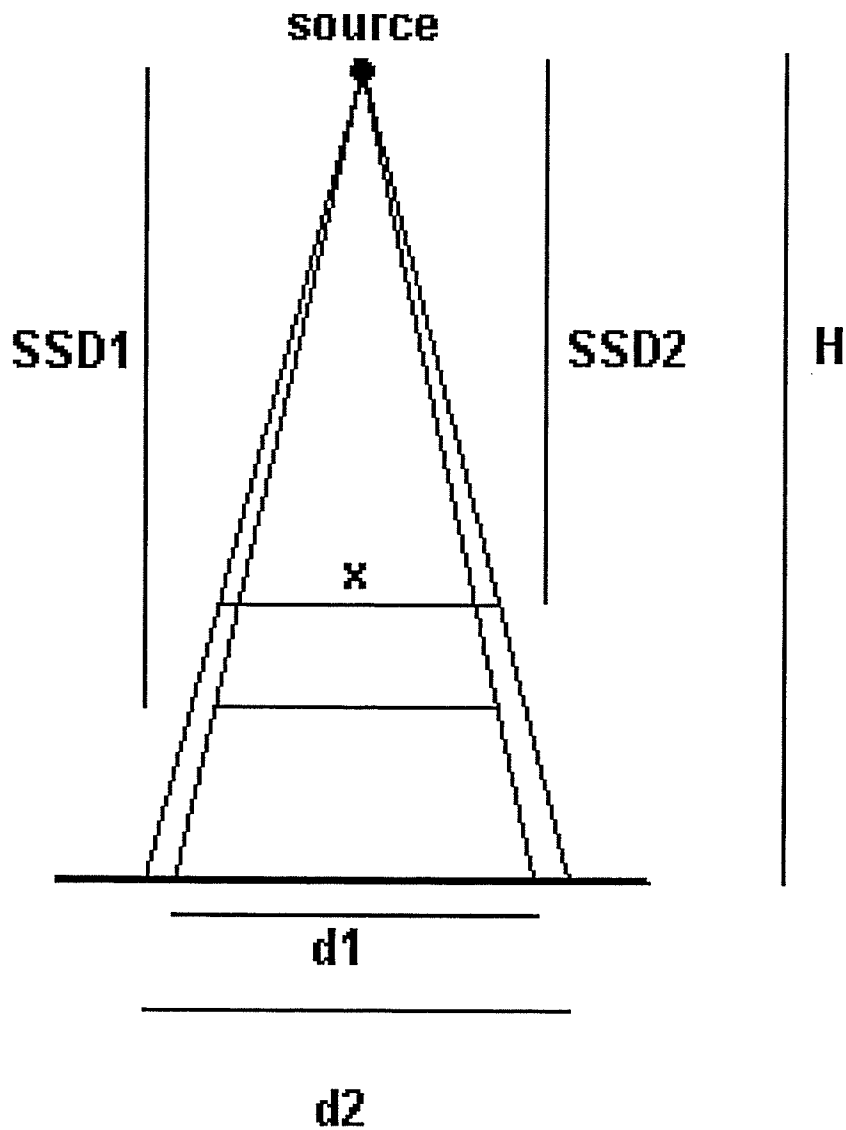


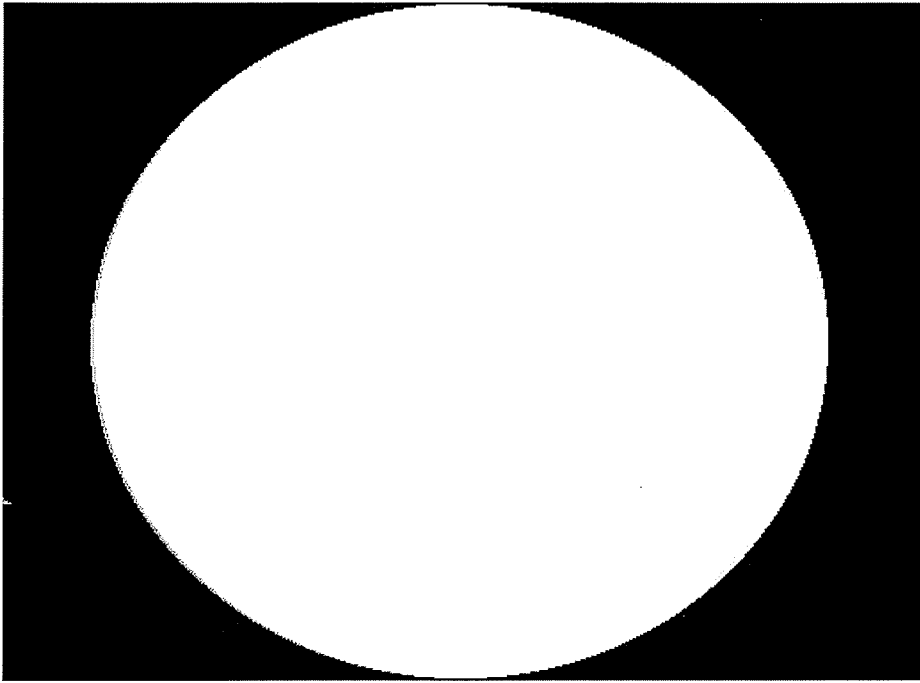
Figure 4.2 An example of a treatment deviation. The prescribed source to surface distance (SSD1) is 100 cm and the incorrect set up is 80 cm (SSD2).

The scaling of the images is done with “`imresize(I,s)`” function of MATLAB which is provided in the Image processing toolbox of this software. In this function, “`T`” is the matrix of the image and “`s`” is the scale factor. The rotation of the image also can be done with another function in the image processing toolbox of MATLAB, “`imrotate(I,a)`”. In

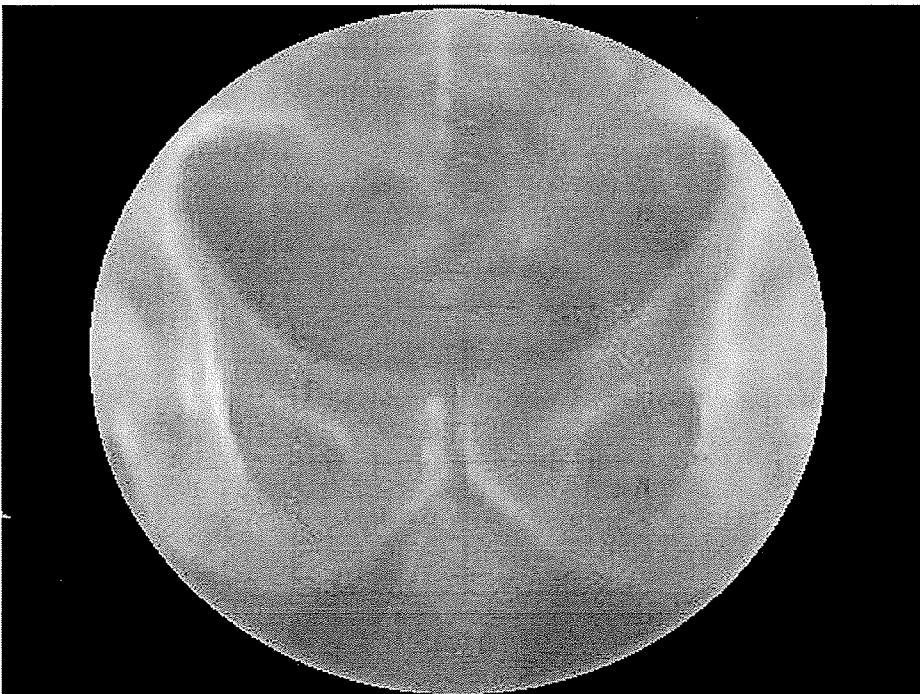
this function “ T ” is the image and “ a ” is the angle of rotation. The angles in MATLAB are expressed in units of “radians”. For translation or cropping the images “`imcrop(I,rect)`” function of MATLAB can be used. In this function, “ T ” is the matrix of the image and “`rect`” has 4 elements indicating the geometry, width and height of the cropped image.

4.2 Reducing sidelobe artifacts in the Fourier domain

Because images are finite, a common artifact that is present in Fourier analysis is the appearance of sidelobes. These artifacts can be seen in Figure 2.1 in each Fourier representation of a simple rectangular figure. The artifacts form the cross-shape spectrum that can be seen in this same figure. This effect is called “tiling” and can be addressed by the use of a circular window and by blurring the edges of the image frame. Figure 4.3(a) illustrates a simple filter, which can be used to reduce the sidelobe effects [5]. This filter contains a circle with values of zero outside the circle and ones inside. Figure 4(b) shows the reference portal image after such filtering. Morgan also identified another filter that can be used for this purpose [5] and he proposes the use of the Blackman window, which is a circular window with blurred edges. It should be noted that there are a good number of possibilities for defining a window that can alleviate these effects. An excellent reference for these windows can be found in [6] and the selection of any of those is based on the tradeoff that exists on reducing the sidelobe level at the expense of reducing resolution in the frequency domain. Due to the complexity of the images in this thesis, this selection is not trivial and future research could evaluate the use of different windows for this application.



(a)



(b)

Figure 4.3 The shape of the filter which is used to reduce the sidelobe artifact (a). The reference image after filtration is illustrated in (b). The pixels of the image outside of the circle become zeros and the pixels inside the circle remain unchanged.

4.3 Results for recovering of in-plane parameters

4.3.1 Scale recovery

The theoretical basis for calculating the scale signature has already been discussed in section 3.3. Fast Fourier Transforms (FFT) were calculated for the reference and test images. For each image, the magnitude of FFT was converted to the log-polar domain and a two-dimensional linear interpolation was used to calculate the scale signature.

The recovered scale factors shown in Table 4.1 reflect the average of the recovered scales for each set of the test images rotated with respect to the reference image. The error in scale recovery according to a wide range of change in rotation is better than 0.04. The data in Table.1 also are plotted in Figure 4.4. The error bars in this figure are equal to $\pm 1\sigma$. Fitting a linear function to the recovered scales, gives a line with a slope of the 1.16.

Table 4.1 Results for scale factor recovery.

Actual scale	Measured scale	One Standard deviation	Error
0.86	0.83	0.08	0.03
0.93	0.91	0.03	0.02
1.00	0.99	0.02	0.01
1.07	1.06	0.01	0.01
1.14	1.15	0.02	0.01
1.21	1.23	0.03	0.0
1.28	1.32	0.06	0.04

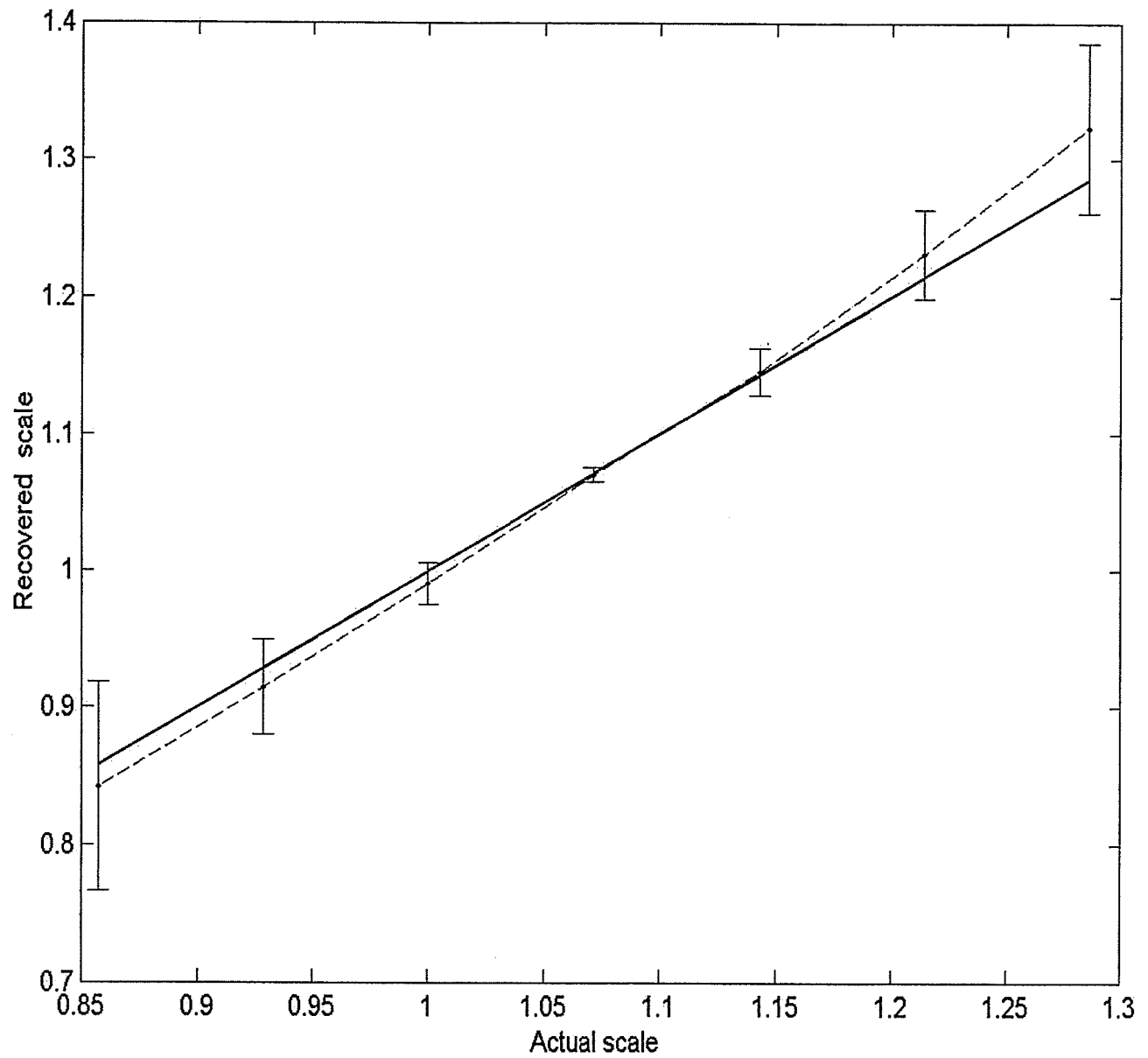


Figure 4.4 The plot of recovered scale factor versus actual scale. The solid line with a slope of one represents the actual amount of the scale factor and the dashed line represents the recovered scale factor with related error bars.

There are significant errors for the large scale factors since parts of the image go outside of the frame. Also for scale factors less than one, new parts come into the image frame and error is increased with decreasing of scale factor. This is illustrated in Figure.4.5, which plots the magnitude of error in scale recovery for all of test images. In this figure for each specific rotation, as the scale increases or decreases the magnitude of the error is increased.

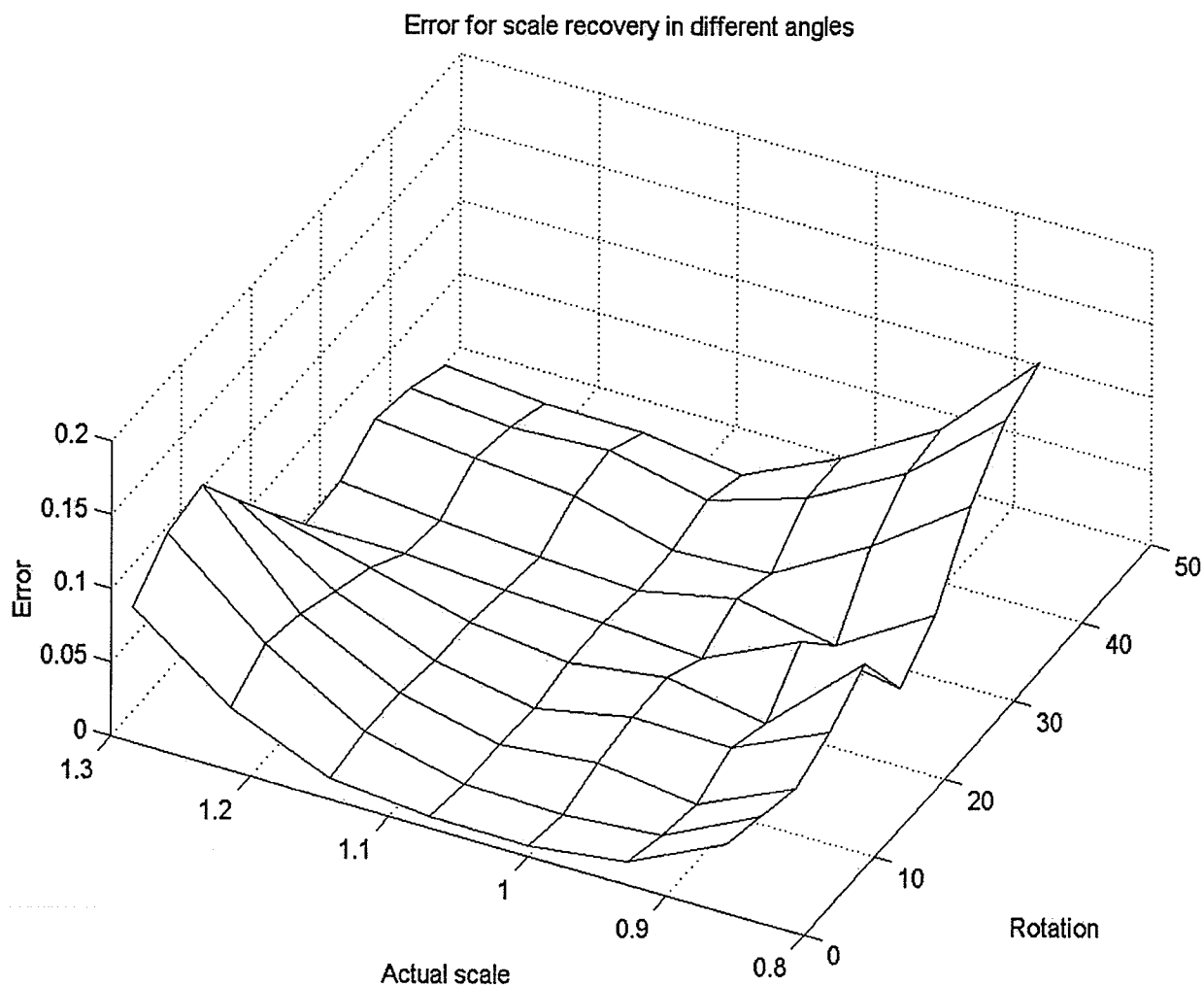


Figure 4.5 Absolute value of the error for scale recovery of the test images. The numbers in horizontal axes are related to the scale factor and rotation angle of each test image with respect to the reference image.

For an infinite frame or for cases where the frame encompasses the whole image, (Figure 4.6) and no new parts come into the frame due to scaling, there is less discrepancy with decreases in the scale factor. For the image in Figure 4.6, the upper limit of the recovered scale factor is greater because for large scaling only a small part of the image goes outside of the image. Table 4.2 illustrates the result for scale recovering using Figure 4.6 as the reference image. For the scale factor up to the 1.4 no part of the image goes outside of the frame even at large angles, so the algorithm can recover the scale factor with very good accuracy.

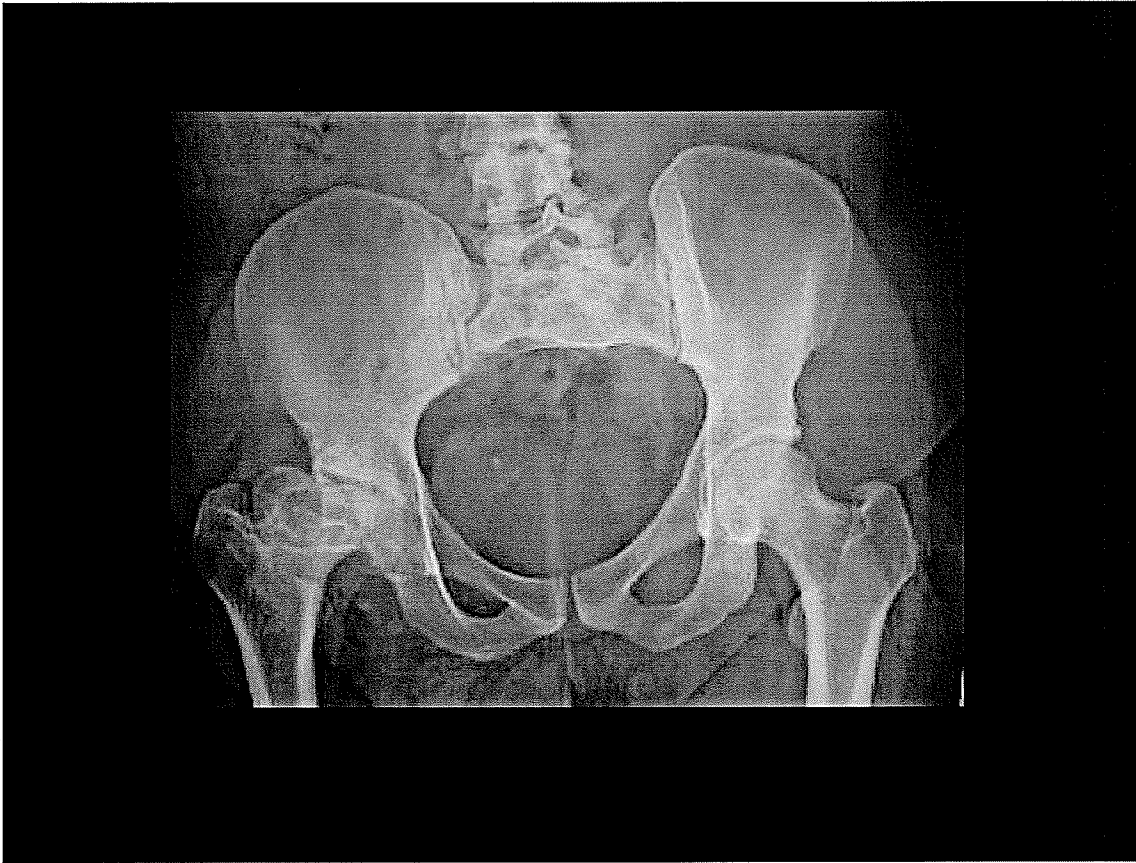


Figure 4.6 X-ray image of the pelvis encompassed by a larger frame

Table 4.2 Scale recovery for the x-ray image of pelvis

Actual Scale	Measured scale	One Standard deviation	Error
0.4	0.4	0	0
0.8	0.8	0.02	0
1.0	1.0	0.0	0
1.2	1.19	0	0.01
1.4	1.41	0	0.01
1.8	1.81	0.11	0.01
2.0	1.93	0.14	0.06

4.3.2 Rotation recovery

Table 4.3 illustrates the results for rotation recovery. The measured rotation is the average of recovered rotation values for the test images with different scales. There is no specific relation between the magnitude of discrepancies and the magnitude of the rotation. In the scale recovery the discrepancies are increased with large scales but for rotation recovery there is less discrepancy, especially for the larger angles. The reason is that during a rotation some parts of the image that may have a large effect in the frequency domain and rotation signature, such as the edges, remain out side of the frame. The magnitude of this effect does not depend on angle of rotation but depends on the specific structure of each image. So the discrepancies do not necessarily happen at large angles. The variations are due to an important part of the image going outside of the image at one particular angle and returning to the image frame at a larger angle. This can also be seen in Figure 4.5, as there is no regular pattern in the error for each scale in

different rotations. For example in Figure 4.5, the large errors for 0.86 scale lies in the large angles while for 1.28 the large errors are in small angles.

Table 4.3 Rotation factor recovery

Actual Angle	Measured angle	Standard deviation	Error
5.0	5.64	0.89	0.64
10.0	11.01	1.81	1.01
15.0	16.35	2.23	1.35
20.0	21.81	2.94	1.81
25.0	26.94	3.17	1.94
30.0	30.99	2.72	0.99
35	34.70	2.34	0.30
40	38.81	1.48	1.19
45	43.1	1.06	1.9

The results in Table 4.3 are plotted in Figure 4.7, where the dotted line is the ideal results having a slope of one and the solid line is the fitted line to the results with a slope of 0.92 and a correlation coefficient of 0.995. It can be seen that with the expectation of the larger angles the error bars are within one standard deviation with the result .

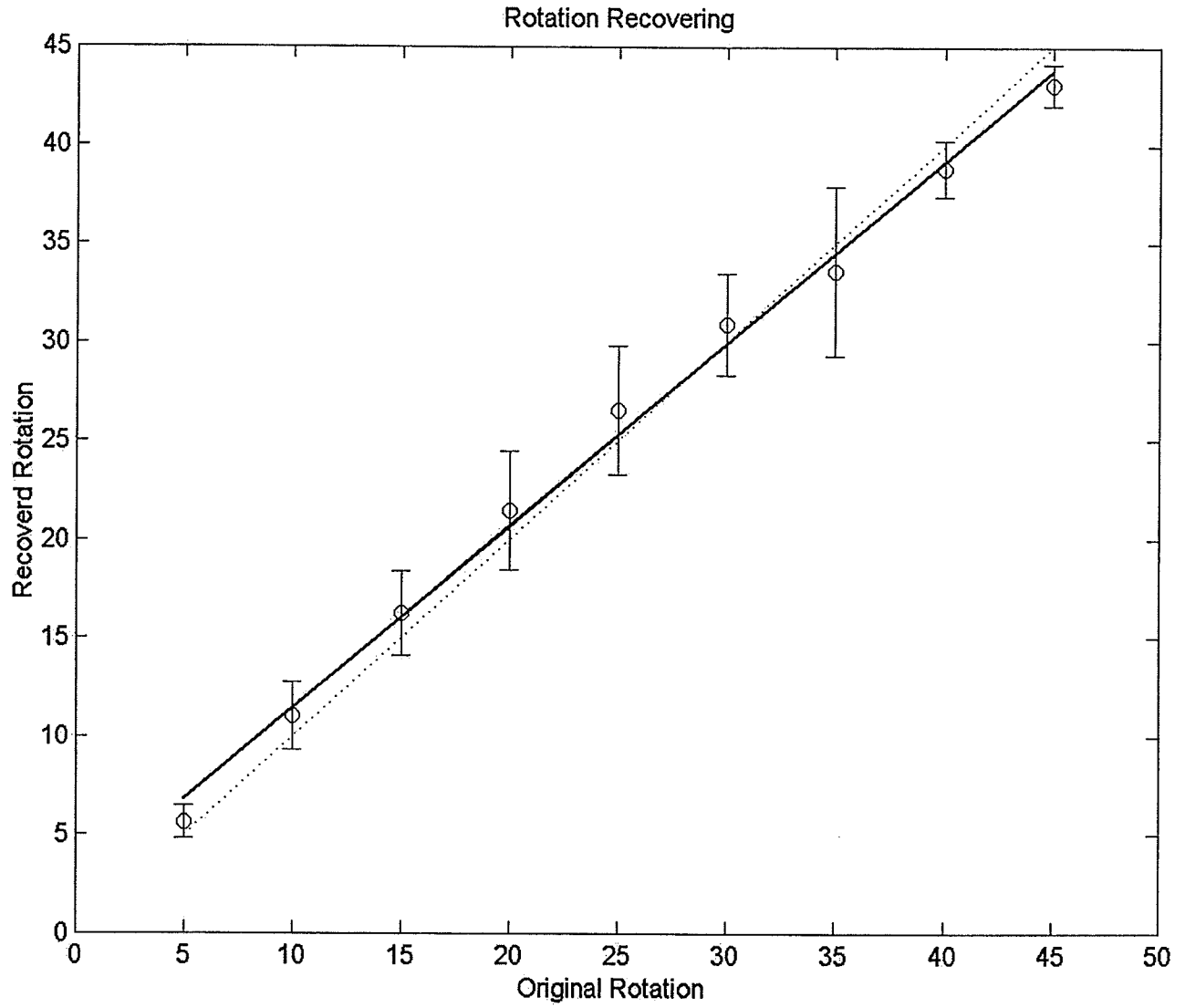


Figure 4.7 The results for rotation recovery. The recovered results are shown with circles. The dotted line with slope of one represents the ideal rotation angle and the solid line represents the recovered rotation angles with related error bars.

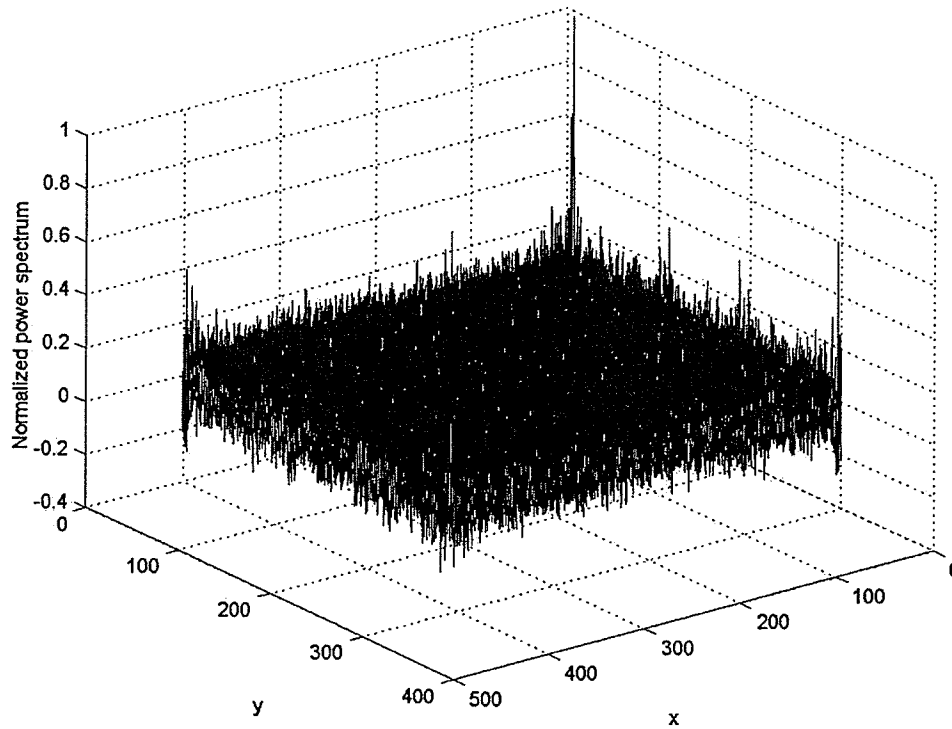
4.3.3 Translation recovery

In our algorithm the results of the translation recovery depend on the error in rotation recovery. According to section 2.4, translation recovery is done after finding the scale and rotation factors and then correcting for these two transformations.

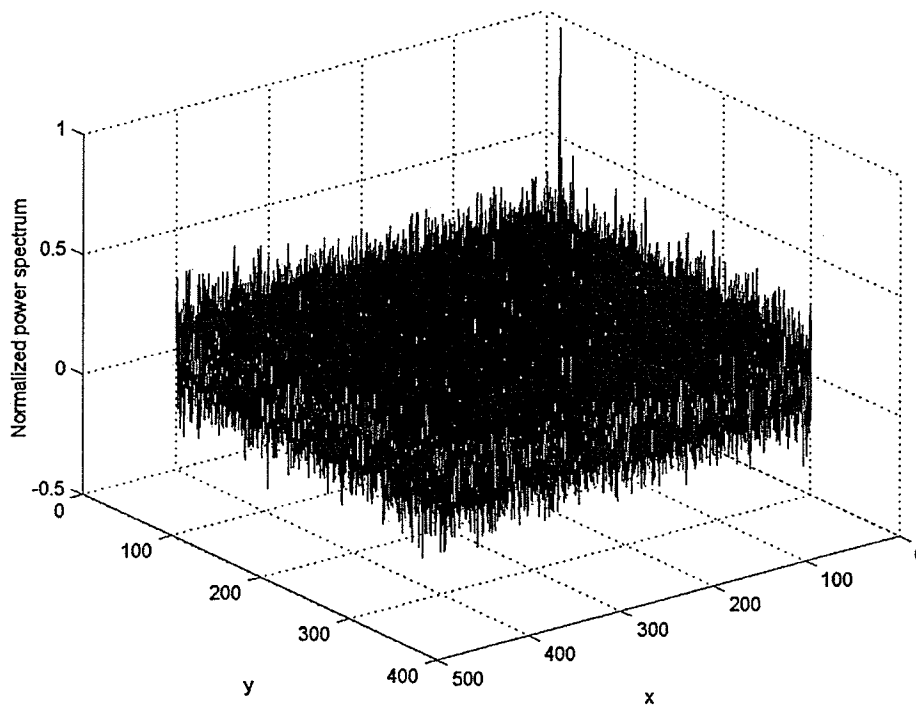
Figure 4.8 is an example of the normalized cross power spectrum of two test images, as discussed in section 3.5. Figure 4.8(a) and (b) are related to the images, which are translated with respect to reference image by a magnitude of (10,20) and (18,36) in x and y directions respectively. For both images the rotation factors are recovered with 5° error so after correcting the rotation the images are not exactly the same as reference image. As we see in the power spectrum, even in the presence of 5° rotations, there is still a clear peak with respect to the reference image. When comparing the position of the peaks in Figure 4.8(a) and (b), the shift of the peaks due to the translation is also recognizable. As the translation parameter increases and as the magnitude of the error in rotation parameter increases the background peaks increases. The background peaks are related to the points that the algorithm finds a match between two images. After a certain limit the background peaks reach the limits of the main peak. At this point the algorithm cannot recognize the location of the main peak. The limits in our algorithm are 40 pixels for translation parameters and 5° for rotation error. So after undoing the effect of rotation, if the images are still rotated with respect to each other with less than 5° it is possible to recover the magnitude of the translation parameters.

We found that as long as the rotation is recovered within 5° of accuracy, the translation parameters in x and y dimension within the range of 0 to 40 pixels can be recovered with an accuracy of ± 1 pixels. Since we are able to extract the rotation with an accuracy better than 3° , the algorithm is able to recover the translation factor with ± 1 pixels.

The magnitude of the error in scale recovery within the range 0.8 to 1.2 had no effect in the accuracy of translation recovery.



(a)



(b)

Figure 4.8 The normalized Cross Power Spectrum related to two test images after scale and rotation recovery with 5° error in rotation recovery. a) The cross power spectrum of an image which has translated (10,20) in x and y direction with respect to the reference image. b) The cross power spectrum for translation of (18,36) pixels in x and y respectively.

4.4 References

1. B. S. Reddy and B. N. Chatterji, "An FFT-based technique for translation, rotation, and scale invariant image registration," *IEEE transactions on image processing* **5**, 1266-1271 (1996).
2. P. Munro, "Portal imaging Technology, past present and future," *Seminars in Radiation Therapy* **5**, 115-133 (1995).
3. J. Bijhold, "Three-dimensional verification of patient placement during radiotherapy using portal images," *Med. Phys.* **20**, 347-356 (1993).
4. Mc G. Morgan "An image registration technique for recovering rotation, scale and translation parameters." *NEC Tech Report* (1998).
5. S. H. Stone, B Tao, and Mc G Morgan. "Analysis of image registration noise due to rotationally dependent aliasing," *J. Vis. Commun. Image.* **14** 114-135 (2003) pp.
6. F. J. Harris." On the use of windows for harmonic analysis with the discrete Fourier transform". *Proceedings of the IEEE*, **66**, 51-83 (1978).

5 Recovery of out-of-plane rotation

5.1 Introduction

Quantification of patient rotations in planes nonparallel to the plane of the EPID, out-of-plane rotations, is difficult because of the two dimensional (2D) nature of portal images. The inability to quantify these rotations creates several problems. First, analysis of one or multiple fields in 2D yields incomplete information that can be difficult to transfer to a setup error in three dimensions (3D) required for correction. This is particularly true for non-orthogonal beams [1]. Second, the ability to measure deviations in a patient setup in 3D is desirable to examine the frequency, extent, and effect of out-of-plane rotations, to improve setup protocols and to assess the effectiveness of immobilization devices. Third, correct interpretation of patient alignment in 3D yields necessary information for the comparison of planned dose with delivered dose [2]. Such a comparison could provide essential knowledge of the effect of misalignments on the treatment outcome. Another problem with analysis in 2D is the risk of interpreting out-of-plane rotations as translations, which affects the reliability of 2D alignment tools [3-4]. This problem may impede further improvement of the accuracy for some treatment sites.

A number of groups have reported on techniques to analyze the setup of a patient in 3D using anatomic [5-7] or artificial landmarks [8-10]. The success of the-former methods depends strongly on the ability to identify specific anatomic structures in portal images. Methods based on implanted radio-opaque fiducials generally show good accuracy but have the disadvantage of requiring a surgical intervention. Externally placed

markers have also been used [9,10]. J. Bijhold *et al* has investigated the three-dimensional verification of patient placement during radiotherapy using portal images [3]. Because portal and simulator images do not give complete information about the three-dimensional position of anatomical structures in the patient, as for instance images of a CT scan do, comparing these images can only yield limited information. In the same study, a method was presented for the determination of the three-dimensional translation and one rotation, in the plane perpendicular to the central beam axis, using only a portal and a simulator image. Measurements on a pelvic phantom showed that accurate determination of patient placement with such a method is only possible for translations smaller than 1 cm, while out-of-plane rotations (rotations in other planes) should be smaller than 2°.

Instead of using a simulator image, one can also use digitally reconstructed radiographs (DRRs), computed from CT scans. Out-of-plane rotations in patient setups with head-and-neck fields were estimated with an accuracy of 2° by comparing a portal image with a series of DRRs computed using different estimations of the out-of-plane rotation [11]. This approach requires, however, a large computation time.

In section 1.6 we reviewed two methods based on anatomical landmarks and artificial markers. Our registration method is based on anatomical structures, but the artificial markers can also be used for image registration.

5.2 First approximation for image registration

5.2.1 Introduction

In this study the possibility of recovering the out-of-plane rotation using a single portal image was evaluated. Previous work show that the detection of out-of-plane rotation is based on images from two three beams perpendicular to each other [section 1.5]. This hypothesis is not applicable for online treatment sessions, because in a real treatment session there is only a single portal image at each time. It is possible to use some information from digitally reconstructed radiographs (DRRs) or CT, which can be provided before treatment. However this work will show online treatment verification can be done using just a single portal image from the patient. We will start with an approach that is based on simple assumptions, which then progresses to more complicated cases.

As shown in Figure 5.1 the reference image is an anterior posterior image of the pelvis (Figure 5.1).

In the first approximation there are two assumptions:

- 1) The anatomical structures are in the same plane.
- 2) The beams are parallel.

According to these assumptions all of the anatomical structures are at the same depth. The second assumption is applicable to the cases that distance between the anatomical structures or artificial landmarks like implanted markers are small with respect to the source to surface distance.

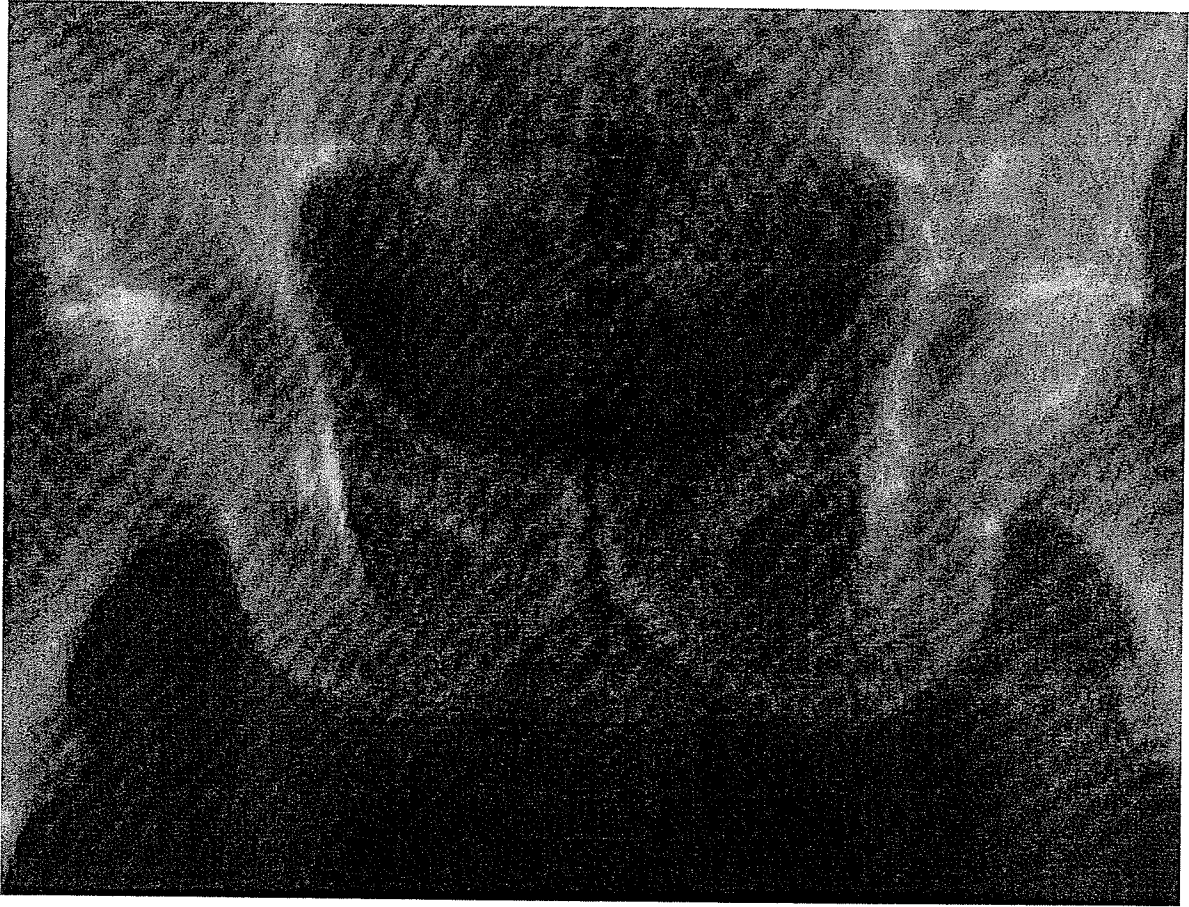


Figure 5.1 Anterior-posterior view of the pelvis image as a reference image for the first approach

5.2.2 Mathematical properties of out-of-plane rotation

With parallel beams, the effect of an out-of-plane rotation of an object in a 2 dimensional image can be predicted mathematically. Figure 5.2 shows a simple configuration of an object. This corresponds to the assumptions from the first approximation, that the structures are in the same plane and are irradiated with parallel beams, coming from the Z-axis.

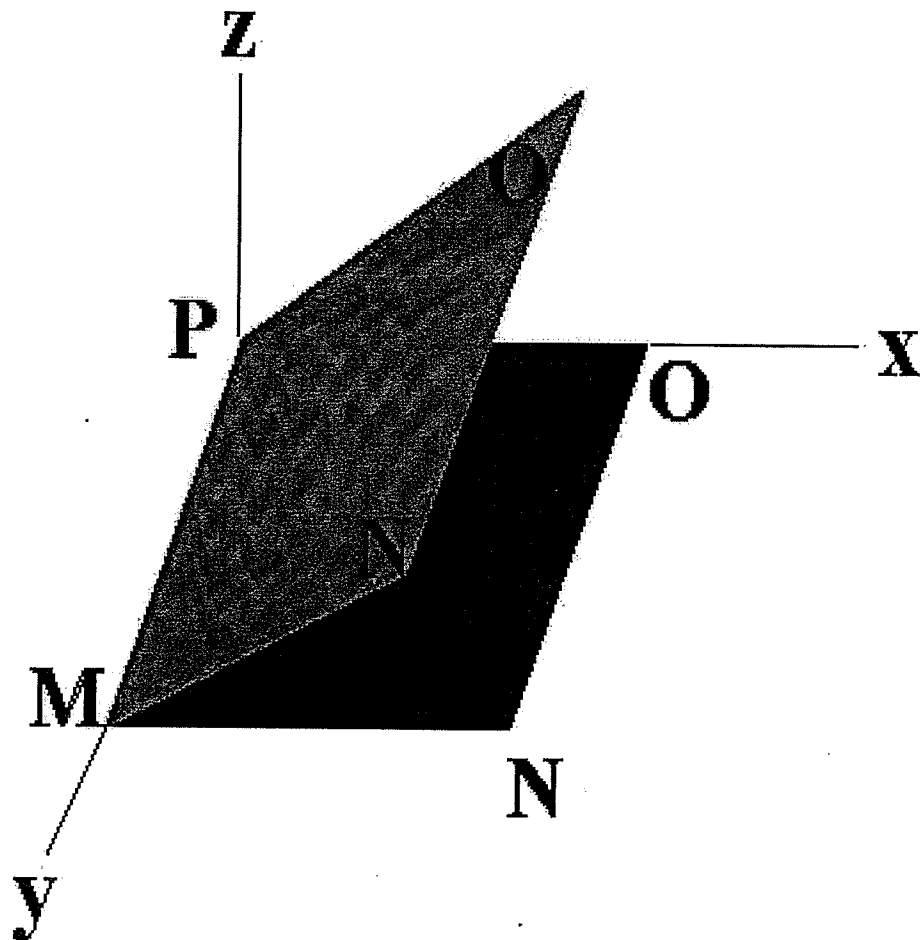


Figure 5.2 The beam originates from a perpendicular direction to the X-Y plane, in the opposite direction of the Z-axis. The object (MNOP) is illustrated before and after rotation.

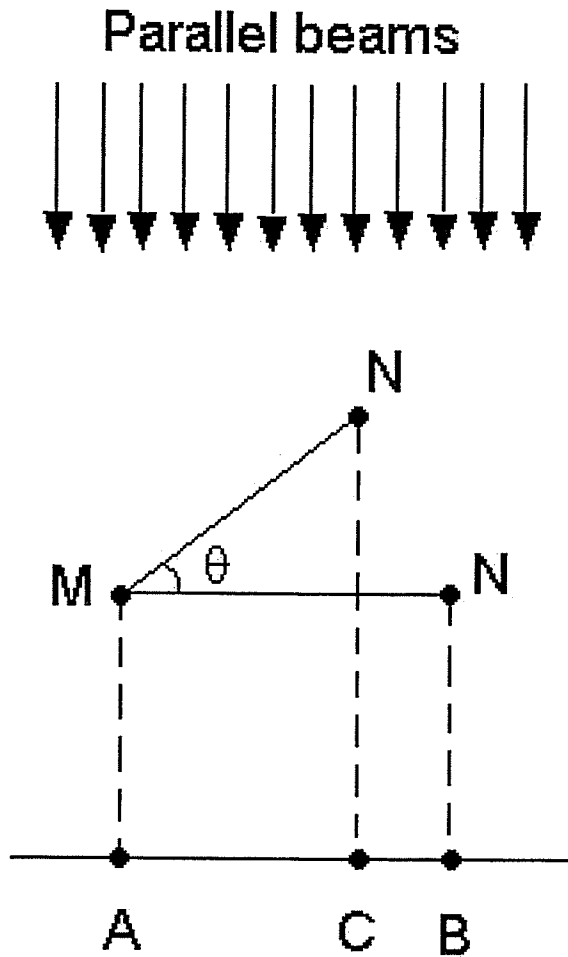


Figure 5.3 Illustration of the mathematical properties of out-of-plane rotation in the presence of a parallel beam.

As illustrated in Figure 5.2, if one examines the X-Z plane from the Y-axis, one sees the results presented in Figure 5.3. In Figure 5.3, AB is the initial image of the object (MN) and AC is the image of the object after the out-of-plane rotation. The magnitude of out-of-plane rotation is θ . According to this figure, the length of the images of the object before and after rotation in this particular direction are related by:

$$\begin{aligned}
 AB &= MN \\
 AC &= MN \cos \theta
 \end{aligned}
 \tag{5.1}$$

For magnification in this particular direction:

$$\frac{AC}{AB} = \cos \theta \quad (5.2)$$

So magnification in this particular direction is equal to $\cos \theta$, where

$$M_x = \cos \theta \quad (5.3)$$

For magnification in the Y direction one follows the same approach. As illustrated in Figure 5.2, if one examines the Y-Z plane from the X-axis one sees the results presented in Figure 5.4.

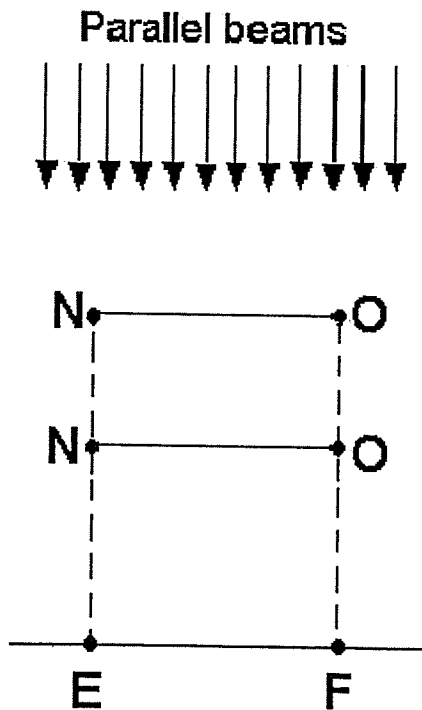


Figure 5.4 The geometry of the object in the Y-Z plane before and after out-of-plane rotation illustrated in Figure 5.2

In the y direction, the beams are always perpendicular to the lines in the y direction even after rotation. There is no difference between the dimension of the object and its image in the y direction before and after rotation. Therefore the magnification in Y direction is unity:

$$M_Y = \frac{EF}{EF} = 1 \quad (5.4)$$

One of the common problems in detecting out-of-plane rotation is that it can be confused with a translation. One way to detect whether there is an out-of-plane rotation is to consider the ratio of the magnification in the X and Y directions. Combining Eq. 5.3 and Eq. 5.4 gives:

$$M_{XY} = \frac{M_x}{M_y} = \cos \theta \quad (5.5)$$

So if one extracts the ratio of the scale factors, by taking the inverse cosine of that ratio, the magnitude of an out-of-plane rotation can be recovered. In the case of the in-plane translation M_x and M_y are unity and the ratio of them M_{xy} will be one.

5.2.3 The results for first approximation

In section 2.2.4, it was illustrated that it is possible to extract the scale factors in horizontal and vertical directions separately using the Fourier transform of the image. This property of the Fourier transform enables the extraction of the magnitude of the out-of-plane rotation.

A set of test images was generated using the reference image (as shown in Figure 5.1). Four of the test images are shown in Figure 5.5. In these images it is assumed that the out-of-plane rotation is in the form of patient roll. As expected there is no change in the vertical dimension of the images. The MATLAB software has the capability of scaling an image in the horizontal and vertical dimensions separately. This is done in MATLAB with the “*imresize(I,[a b])*” function , in which “I” is the image, “a” is the scale factor in the vertical dimension and “b” is the scale factor in the horizontal dimension.

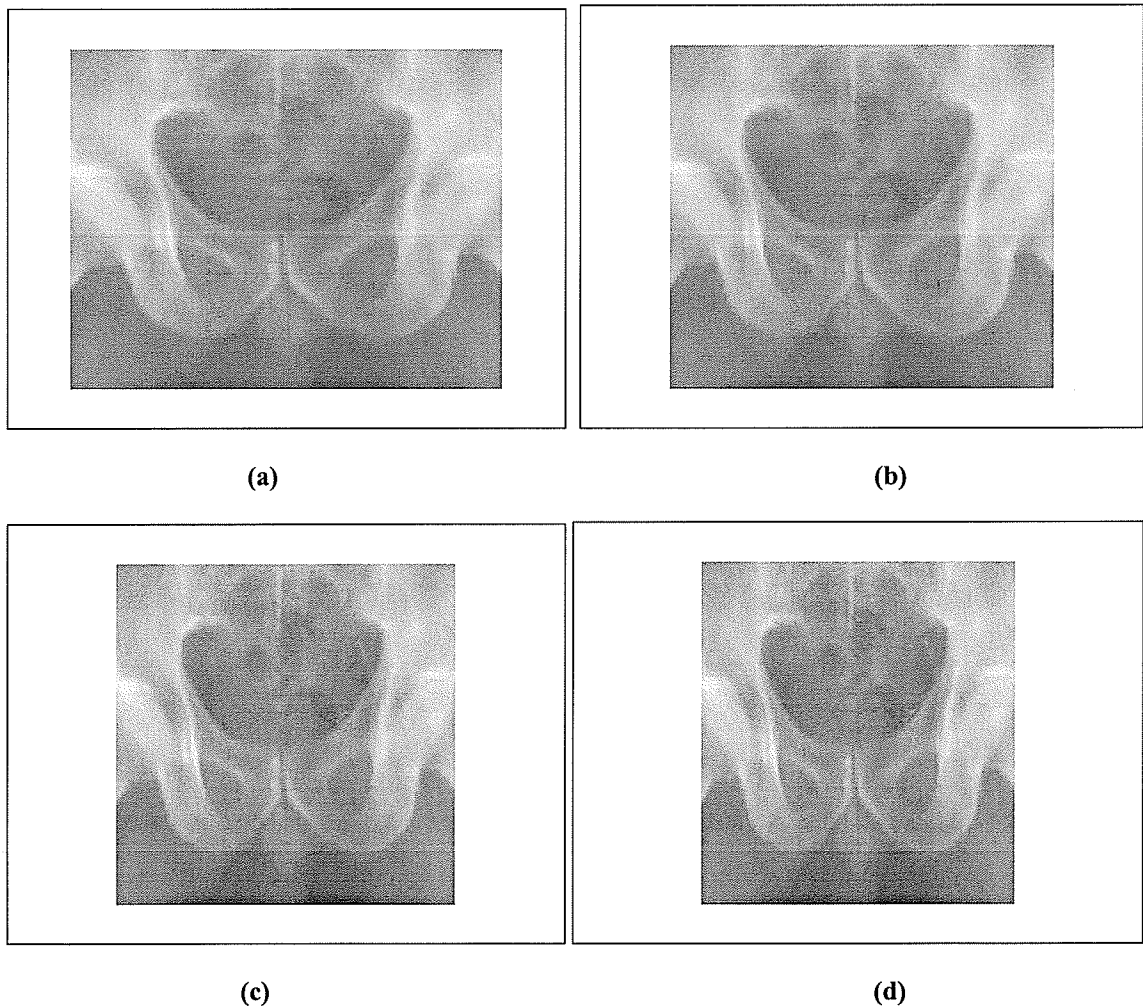


Figure 5.5 Four samples of the test images with rotation of 18°(a), 33°(b), 42°(c), 48°(d) around the vertical axis.

In the algorithm for out-of-plane rotation recovery, the first step was to take the Fourier transform of a test image and a reference image. In the second step the Fourier Transform of the images are transferred to the log domain. Linear interpolation is then used to obtain the needed points from the existing points. The third step involves determining the scale factor in the horizontal direction, which is done by integrating over the vertical axes, leaving a function that depends only on changes in the horizontal direction. This function is called the "horizontal signature". By correlating the horizontal signature of the test image and the horizontal signature of the reference image the magnitude of the shift can be recovered. This is the shift of the Fourier transform of the two images with respect to each other.

According to equation 3.9 the shift is a function of the scale factor. After calculating the scale factor in the horizontal direction, the scale factor in the vertical direction is calculated in the same manner. The ratio of the scale factors is equal to $\cos\theta$ (Eq. 5.5). Finally the inverse cosine of the ratio of the scale factors is used to recover the magnitude of the out-of-plane rotation.

The results of angle recovery for the test images are illustrated in Figure 5.6. The angle of rotation is between 2° and 28° with 4° increments. These results also are shown in Table 5.1. There are large errors at the smaller angles, which is a result of solving for θ for values of $M_x/M_y \approx 1$. These results are for images, assuming the registration of the anatomical structure. This technique could also be used for image registration based on the artificial landmarks.

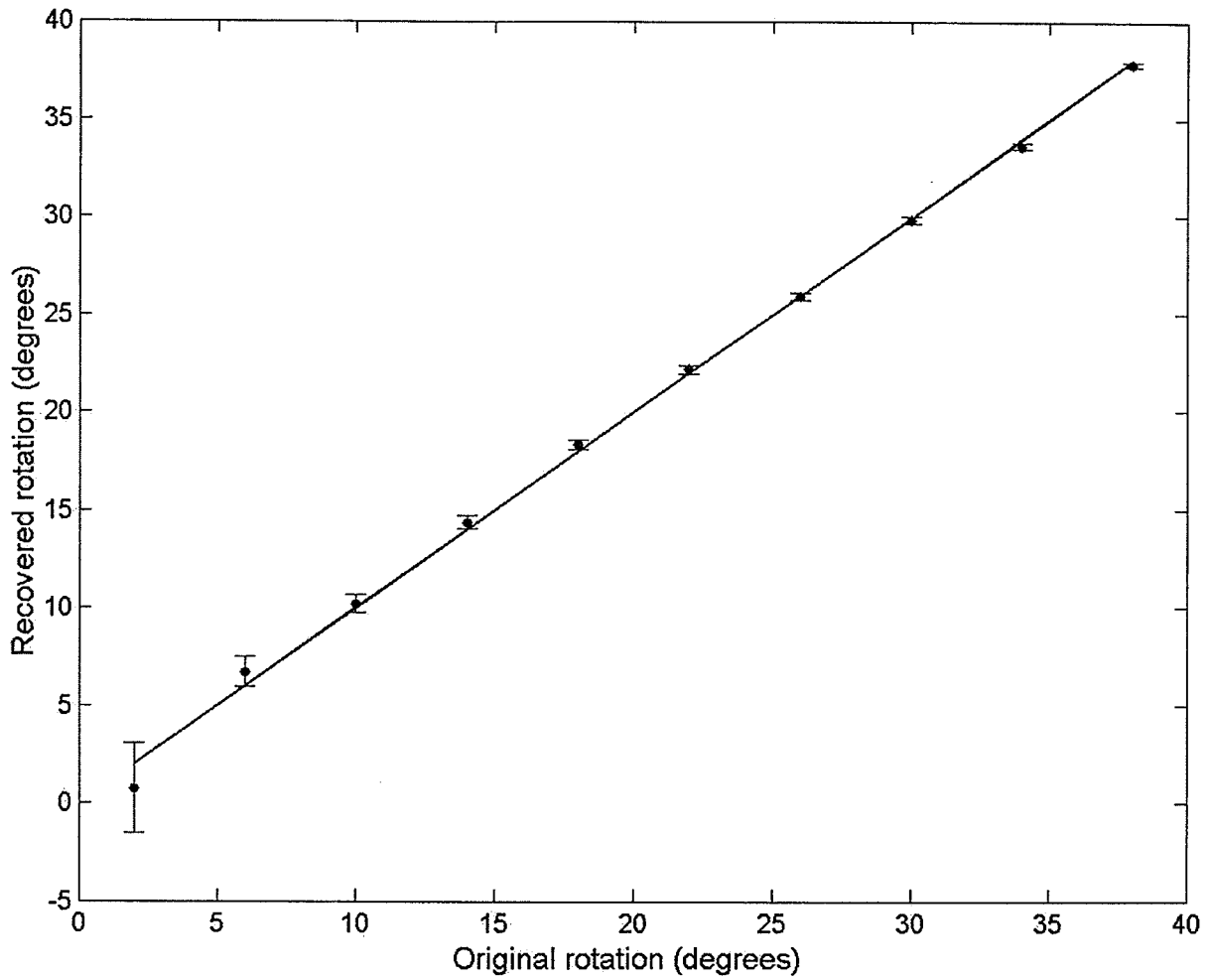


Figure 5.6 Recovered scale factor for test images, which are rotated with respect to the reference image. The ideal results are shown with the solid line. The error bars are related to 50% confidence limits, as discussed in section 5.4.

Table 5.1 Results for Out-of-plane rotation recovery

Actual Angle	Recovered angle	Error
2.0	0.77	1.23
6.0	6.72	0.72
10.0	10.21	0.21
14.0	14.38	0.38
18.0	18.36	0.36
22.0	22.21	0.21
26.0	25.99	0.01
30.0	29.90	0.10
34.0	33.67	0.33
38.0	37.8	0.20

The assumption that the beams are parallel is reasonable in some cases. For treatment verification based on the artificial landmarks, the distance between the artificial landmarks may be of the order of only a few centimeters. For example, if one uses a SSD of 100 cm, and distance of 2 cm for landmarks, the ratio of the anatomical landmarks to this SSD is 2 percent, and the beams can be assumed to be parallel [5].

In this approach, the idea of using the ratio of scale factors to extract the out-of-plane rotation provides information that aids in solving more complicated cases.

5.3 Second approach for image registration

5.3.1 Mathematical issues for the second approach.

The second approach for recovery of out-of-plane rotation is based on a more realistic assumption than the first approach. In this approach, it is still assumed that all of the anatomical structures are in the same plane, but the beams are divergent. The direction of out-of-plane rotation and the reference coordinates are shown in Figure 5.2. But the beams are not parallel and so diverge along the z-axes.

If the image in Figure 5.2 is examined from the perspective of the y-axis axis, the geometry presented in Figure 5.7 is observed. The out-of-plane rotation is considered as a patient roll around y with magnitude of θ . For the parallel beams, the magnification of each part was independent of distance from the point of rotation. This is not generally correct for a divergent beam. As illustrated in Figure 5.7 the magnification factor for an object located at distance of x from the point of rotation is determined using:

$$\frac{x}{SSD} = \frac{d_1}{H} \rightarrow d_1 = \frac{xH}{SSD} \quad (5.6)$$

$$\frac{y}{x} = \sin \theta \rightarrow y = x \sin \theta \quad (5.7)$$

$$\varphi = 90 - \theta - \frac{\alpha}{2} \quad (5.8)$$

$$\beta = 90 + \frac{\alpha}{2} \quad (5.9)$$

$$\frac{x}{\sin \beta} = \frac{x'}{\sin \varphi} \rightarrow x' = x \frac{\sin \varphi}{\sin \beta} \quad (5.10)$$

$$\frac{d_2}{H} = \frac{x'}{h} \rightarrow d_2 = \frac{x'H}{h} = \frac{x'H}{SSD - y} \quad (5.11)$$

$$d_2 = \frac{\sin \varphi}{\sin \beta} \frac{xH}{(SSD - Y)} \quad (5.12)$$

$$\sin \varphi = \sin(90 - \theta - \frac{\alpha}{2}) = \cos(\theta + \frac{\alpha}{2}) \quad (5.13)$$

$$\sin \beta = \sin(90 + \frac{\alpha}{2}) = \cos(\frac{\alpha}{2}) \quad (5.14)$$

$$d_2 = \frac{xH}{SSD - y} \times \frac{\cos(\theta + \frac{\alpha}{2})}{\cos(\frac{\alpha}{2})} \quad (5.15)$$

$$M_x = \frac{d_2}{d_1} = \frac{xH}{SSD - y} \times \frac{\cos(\theta + \frac{\alpha}{2})}{\cos(\frac{\alpha}{2})} \times \frac{SSD}{xH}$$

$$\therefore M_x = \frac{SSD \cos(\theta + \frac{\alpha}{2})}{(SSD - y) \cos(\frac{\alpha}{2})} \quad (5.16)$$

Eq. 5.16) magnification factor in the x direction.

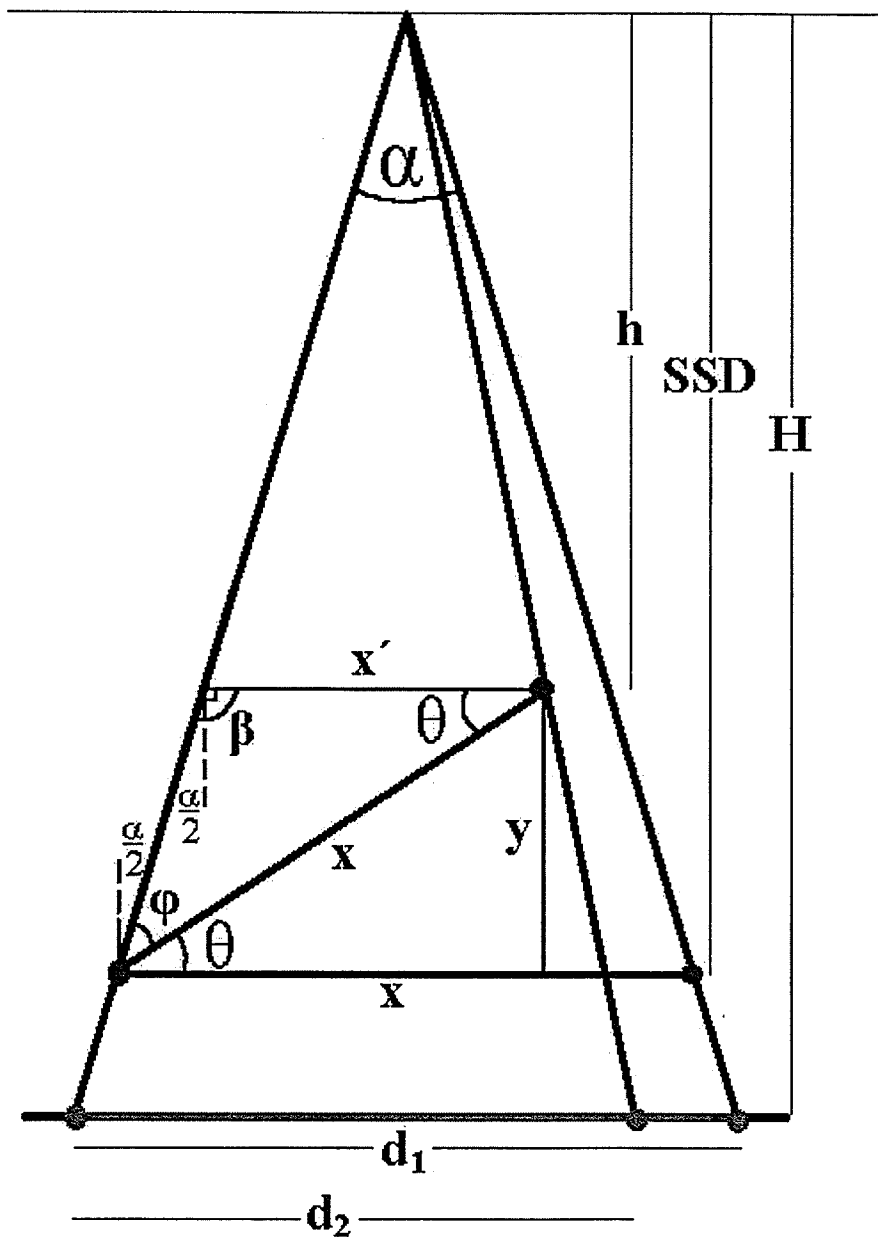


Figure 5.7 The geometry of the beam and out-of-plane rotation considered for the second approach in X-Z plane.

In the next step the magnification factor in the y direction is calculated. If Figure 5.2 is examined from the X-axis perspective, the Y-Z plane geometry as illustrated in Figure 5.8 is observed. In Figure 5.8, SSD, y, h and H are the same as in Figure 5.7. The magnification factor in the y direction is calculated using the following relationships:

$$\frac{d_1}{H} = \frac{b}{SSD} \rightarrow d_1 = \frac{bH}{SSD} \quad (5.17)$$

$$\frac{d_2}{H} = \frac{b}{h} \rightarrow d_2 = \frac{bH}{h} = \frac{bH}{SSD - y} \quad (5.18)$$

$$\frac{d_2}{d_1} = \frac{bH}{SSD - y} \times \frac{SSD}{bH} \quad (5.19)$$

$$M_y = \frac{SSD}{SSD - y} \quad (5.20)$$

M_y is the magnification in y direction. Eq. 5.7 shows that this magnification also depends on x, the distance of the object from the origin of rotation.

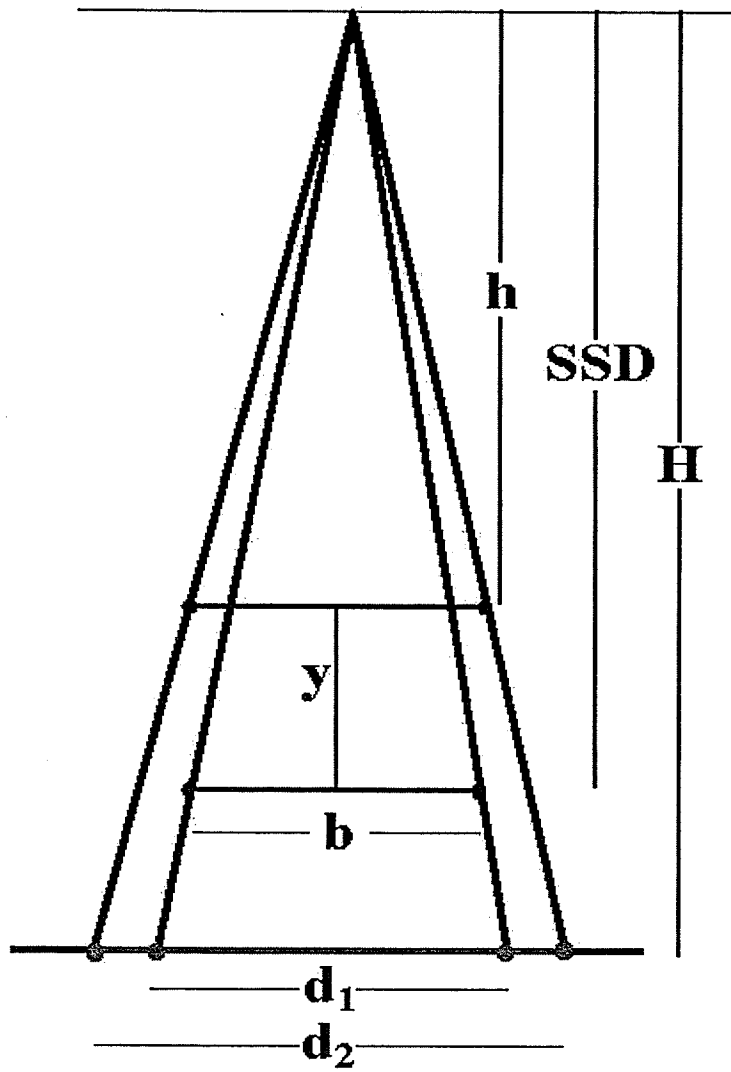


Figure 5.8 The geometry of the beam and out-of-plane rotation considered for the second approach in y-z plane.

If one considers the ratio of magnifications in x and y direction, as given in Eq.

5.16, and Eq. 5.20, we have:

$$\frac{M_x}{M_y} = \frac{SSD \cos(\theta + \frac{\alpha}{2})}{(SSD - y) \cos(\frac{\alpha}{2})} \times \frac{SSD - y}{SSD}$$

$$\frac{M_x}{M_y} = \frac{\cos(\theta + \frac{\alpha}{2})}{\cos(\frac{\alpha}{2})}$$

$$\frac{M_x}{M_y} = \frac{\cos \theta \cos \frac{\alpha}{2} - \sin \theta \sin \frac{\alpha}{2}}{\cos(\frac{\alpha}{2})}$$

$$\frac{M_x}{M_y} = \cos \theta - \sin \theta \frac{\sin \frac{\alpha}{2}}{\cos \frac{\alpha}{2}}$$

$$\frac{M_x}{M_y} = \cos \theta - \sin \theta \tan(\frac{\alpha}{2})$$

$$\therefore M_{xy} = \frac{M_x}{M_y} = \cos \theta - \sin \theta \frac{1}{2} \frac{x}{SSD} \quad (5.21)$$

The ratio of magnifications in x and y is more simple than M_x and M_y , but is still a function of x. As a simple evaluation of Eq. 5.21, a parallel beam has a value of 0 for α , which then yields the result derived in Eq. 5.5.

5.3.2 Approximations and results for second approach

According to Eq. 5.21, M_{xy} for each part of the image depends on its location with respect to the origin of the rotation, and it is difficult to find a general description for a Fourier transform of the image. On the other hand, the Fourier transform of an image after an out-of-plane rotation, depends on that particular image. In order to solve this problem the effect of the second part of Eq. 5.21 is evaluated.

If the maximum possible magnitude for x is x_m , we assume that x/SSD in Eq. 5.20 has the constant value of $x_m/2$ (in the middle of the range), so we have :

$$M'_{xy} = \frac{M_x}{M_y} = \cos \theta - \sin \theta \frac{1}{2} \frac{x_m}{SSD} \quad (5.22)$$

M'_{xy} is an approximation and the actual value of M_{xy} , is a function of x, so there is an error in this approximation. The limits of this error are governed by the range of x in M_{xy} which is between 0 and x_m . One needs to evaluate the "order" of the error that this simplification produces. M_{xy} is considered in the cases for which the error is maximum ($x=0$ and x_m). One sees that

$$M_{1,xy} = \cos \theta \quad (5.23)$$

$$M_{2,xy} = \cos \theta - \sin \theta \frac{1}{2} \frac{x_m}{SSD} \quad (5.24)$$

The percentage error due to the approximation (Eq. 5.22) in each case is:

$$e_1 = \left| \frac{M_{1,xy} - M'_{xy}}{M_{1,xy}} \right| \quad (5.25)$$

$$e_2 = \left| \frac{M_{2,xy} - M'_{xy}}{M_{2,xy}} \right| \quad (5.26)$$

These two parameters, e_1 and e_2 , are plotted versus the out-of-plane rotation as illustrated in Figure 5.9. In this graph x_m and SSD are assumed to be 30cm and 100cm respectively.

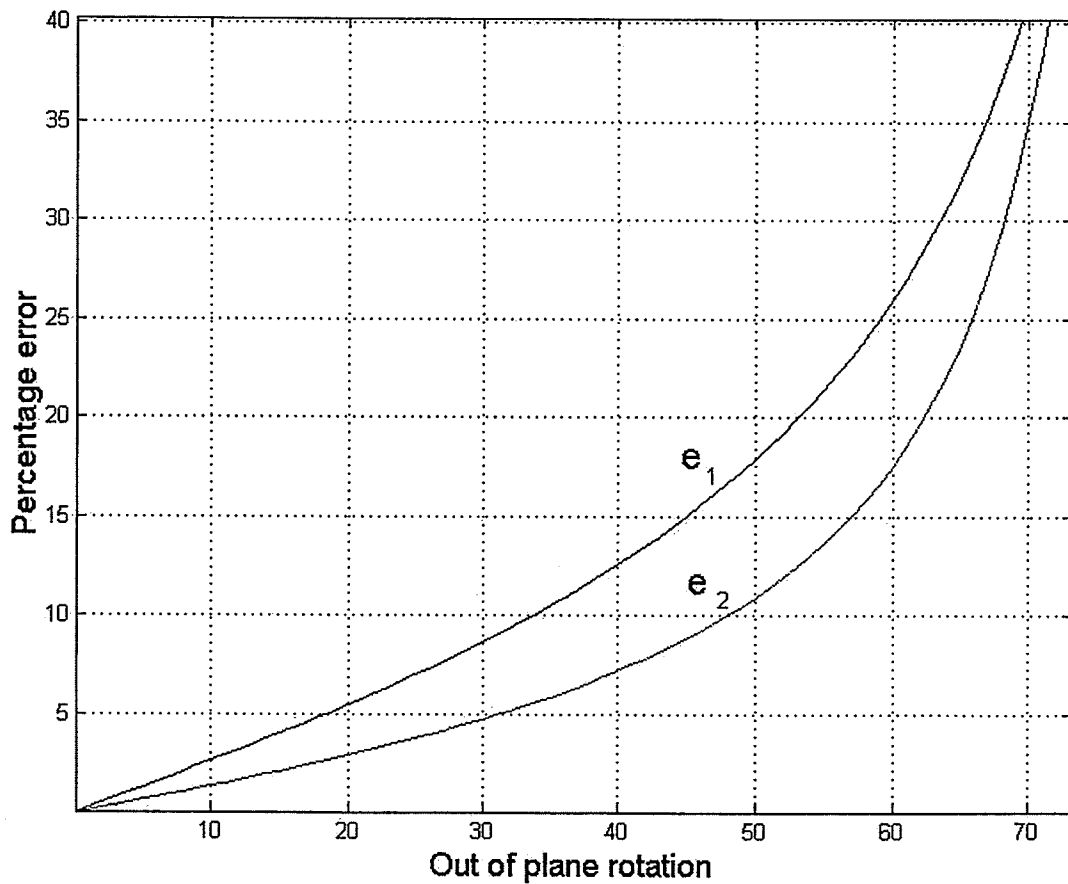
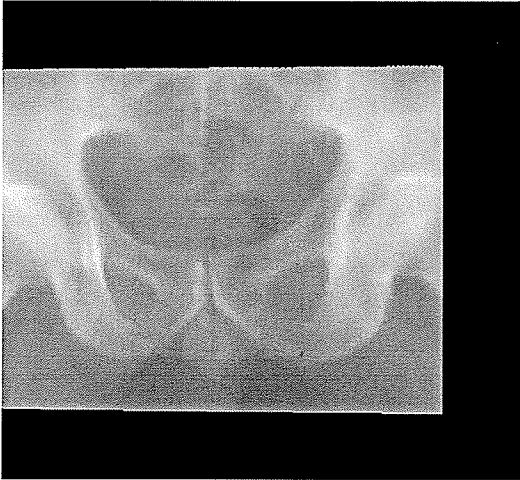


Figure 5.9 The percentage error in calculating the magnitude of M_{xy} according to Eq. 5.24 and 5.45.

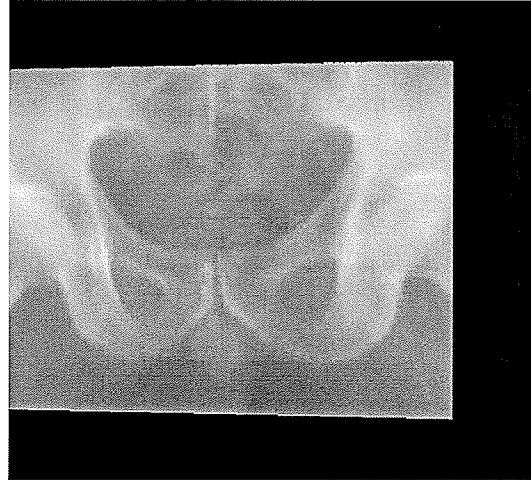
The percentage errors for e_1 and e_2 are below 5 percent for out-of-plane rotations up to 20° . We use this range to test the out-of-plane rotation recovery algorithm.

The reference image for this part is that illustrated in Figure 5.1. The test images were created from this image using Eq 5.16 and Eq. 5.21 and linear interpolation. Four test images are shown in Figure 5.10.

For recovery of out-of-plane rotation, the algorithm of first approximation is used to find the scale factors in the horizontal and vertical directions. The ratio of the scale factors in both directions is calculated and used in Eq. 5.21 to determine M'_{xy} . In both directions, the scale factor for images is not constant and depends on x . However, for angles up to 20° the effect of the term containing the x parameter is on the order of a few percent. The goal was to test the accuracy of the algorithm, given the approximations made in the second approach and equation 5.21.



(a)



(b)



(c)



(d)

Figure 5.10 The test images which are rotated with respect to the reference image 5° (a), 10° (b), 15° (c), 20° (d).

After extracting M'_{xy} for each test image, Eq. 5.22 is solved for θ , yielding

$$\theta = \cos^{-1}\left(\frac{M'_{xy} \pm \sqrt{M'_{xy}{}^2 - \left(1 + \left(\frac{x_m}{SSD}\right)^2\right)\left(M'_{xy}{}^2 - \left(\frac{x_m}{SSD}\right)^2\right)}}{\left(1 + \left(\frac{x_m}{SSD}\right)^2\right)}\right) \quad (5.27)$$

There are two answers for θ , because one needs to solve a quadratic equation. After testing the two answers for a limited case of θ ($\theta=0$ for $M'_{xy}=1$) it was discovered that only the solution that used the positive discernment was valid giving:

$$\theta = \cos^{-1}\left(\frac{M'_{xy} + \sqrt{M'_{xy}{}^2 - \left(1 + \left(\frac{x_m}{SSD}\right)^2\right)\left(M'_{xy}{}^2 - \left(\frac{x_m}{SSD}\right)^2\right)}}{\left(1 + \left(\frac{x_m}{SSD}\right)^2\right)}\right) \quad (5.28)$$

By substituting M'_{xy} into Eq. 5.27, the answers for out-of-plane rotation can be calculated with the results being illustrated in Figure 5.11 and Table 5.2. With the exception of the first point at 2° , all other points have the error increasing with angle. The reason for the larger error for very small angles is that the change in the image is so small that the algorithm can not detect the change accurately.

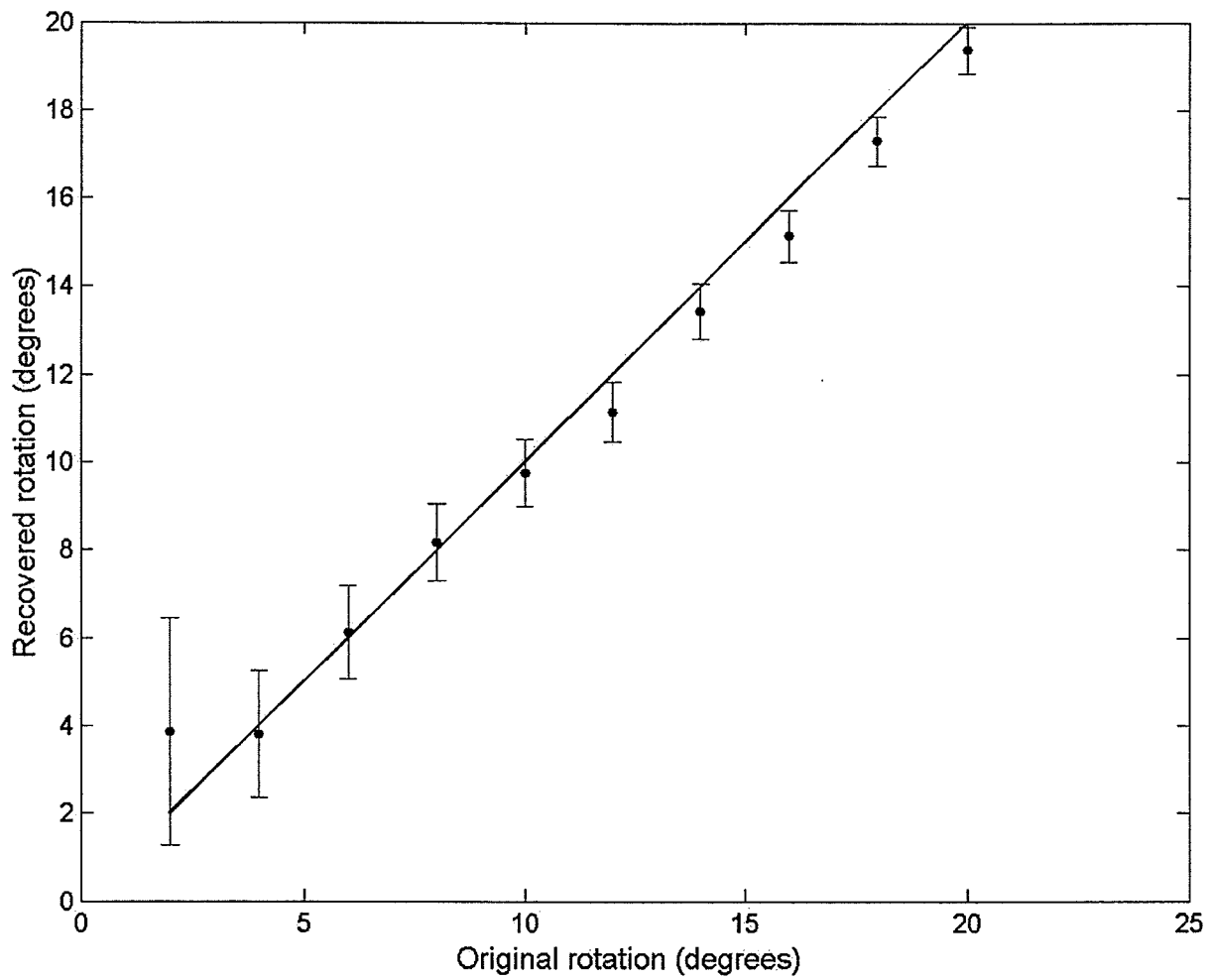


Figure 5.11 The results for extracting the out-of-plane rotation in second approach. The range of angle is between 2 and 20 degrees in 2 degrees steps. The solid line is the ideal answer and the circles are the recovered angles. The error bars are related to 50% confidence limits, as discussed in section 5.4.

Table 5.2 Results for out-of-plane rotation recovery in second approach

Actual Angle	Recovered angle	Error
2.0	3.87	1.87
4.0	3.81	1.19
6.0	6.12	0.12
8.0	8.17	0.17
10.0	9.76	0.23
12.0	11.14	0.86
14.0	13.44	0.56
16.0	15.15	0.84
18.0	17.30	0.70
20.0	19.38	0.62

5.4 Error analysis for recovery of out-of-plane rotation:

In the first and second approaches the magnitude of the out-of-plane rotation is a function of the ratio of the scale factors, M_{xy} (Eq. 5.5 and 5.28). Because M_{xy} is extracted from the Fourier transform of the image and the uncertainties are expressed in the spatial domain, the numerical calculation of the errors is complicated. However, using the first approach it is possible to find a general expression for the magnitude of the error versus angle of rotation and to extract an estimate of ΔM_{xy} for our previous results.

In the first approach we rewrite Eq. 5.5 as:

$$\theta = f_1(M_{xy}) \quad (5.32)$$

Using Eq 5.5 for uncertainty in θ we have:

$$\Delta\theta = \sqrt{\left(\frac{\partial(f_1(M_{xy}))}{\partial(M_{xy})} \times \Delta M_{xy}\right)^2} \quad (5.33)$$

where:

$$\frac{\partial(f_1(M_{xy}))}{\partial(M_{xy})} = \frac{\delta(\cos^{-1}(M_{xy}))}{\delta(M_{xy})} = \frac{\delta(\cos^{-1}(\cos(\theta)))}{\delta(\cos(\theta))} = \frac{\delta\theta}{-\sin(\theta)\delta\theta} = \frac{1}{-\sin\theta} \quad (5.34)$$

Then:

$$\Delta M_{xy} = \left| \frac{\frac{\Delta\theta}{\frac{\partial(f_1(M_{xy}))}{\partial(M_{xy})}}}{\frac{\partial(M_{xy})}{\partial(M_{xy})}} \right| = \left| \frac{\frac{\Delta\theta}{1}}{-\sin(\theta)} \right| = |\Delta\theta \sin(\theta)| \quad (5.35)$$

Using the errors for θ obtained from our experimental results allows us to obtain an estimation for the uncertainty in ΔM_{xy} . Table 5.3 gives the result of substituting the errors ($\Delta\theta$) in Table 5.1 in to Eq. 5.35.

Table 5.3 Results for ΔM_{xy} using Eq. 5.35

Actual Angle	Error	ΔM_{xy}
2.0	0.77	0.042
6.0	6.72	0.075
10.0	10.21	0.036
14.0	14.38	0.091
18.0	18.36	0.011
22.0	22.21	0.082
26.0	25.99	0.004
30.0	29.90	0.045
34.0	33.67	0.184
38.0	37.8	0.123

We assume that ΔM_{xy} is independent of angle and these results are samples from the gaussian distribution of errors in ΔM_{xy} . The average and standard deviation of ΔM_{xy} are calculated to be 0.08 and 0.05 respectively. In order to estimate the uncertainty at the 99% confidence level, a value of ΔM_{xy} equal to 0.21 is used, which corresponds to $\overline{\Delta M_{xy}} \pm 2.57\sigma$. Using this magnitude for ΔM_{xy} , $\Delta\theta$ may be calculated as a function of angle. Figure 5.15 illustrates the results for $\Delta\theta$ versus out-of-plane rotation for both the 99% and 50% confidence limits. The straight line has the slope of one and intercepts the confidence limits at the point at which $\Delta\theta = \theta$. These intercepts occur at angles of $\theta=2^\circ$ and $\theta=3.4^\circ$ for the 50% and 99% confidence limits respectively. This illustrates that we are unable to recover out-of-plane rotations for angles smaller than this.

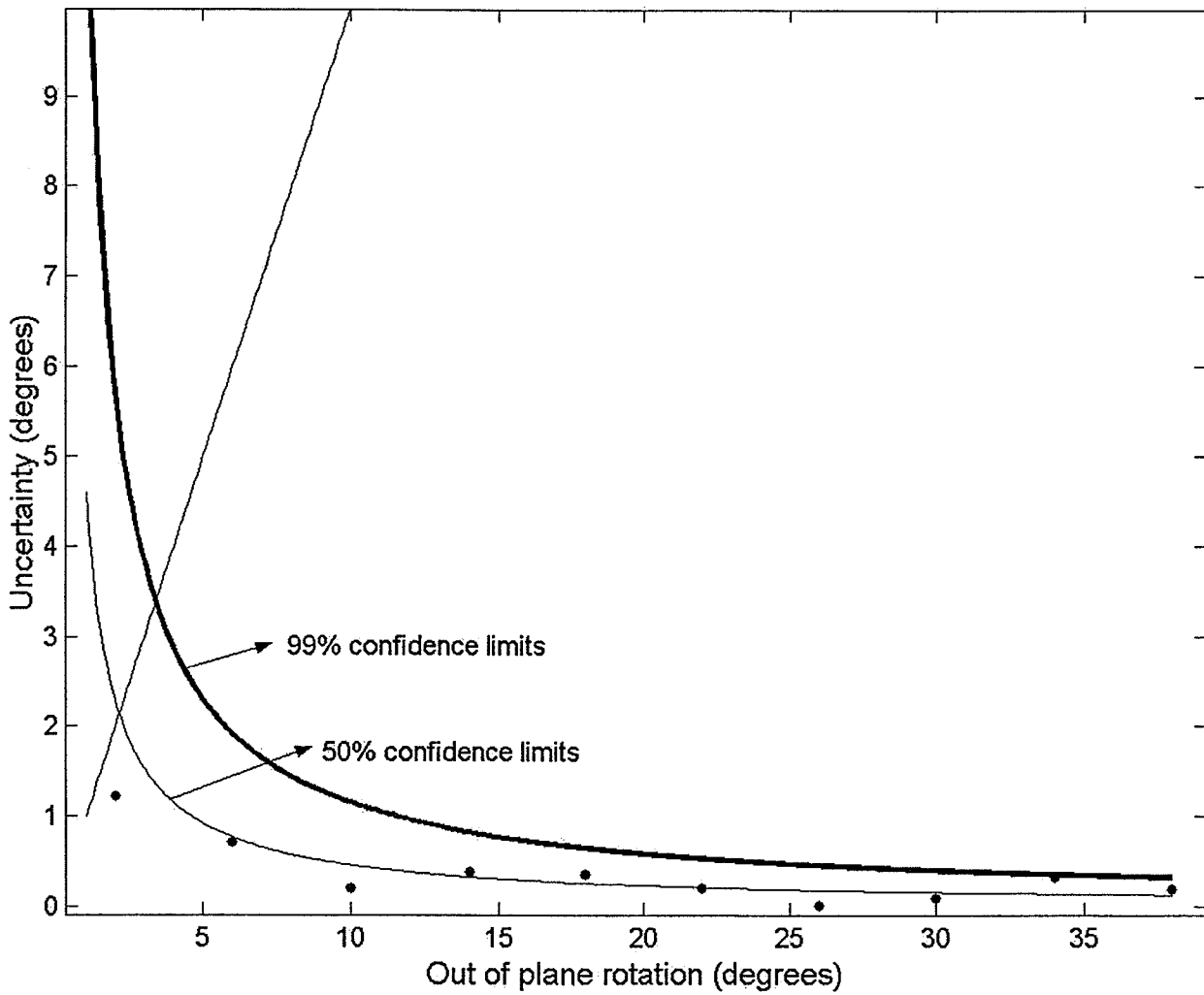


Figure 5.15 The results for the uncertainty versus the out-of-plane rotation. The curves give the 99% and 50% confidence limits of the uncertainties. The straight line represents 45° line in which the uncertainty is equal to the out-of-plane rotation and the dots give results in Table 5.3.

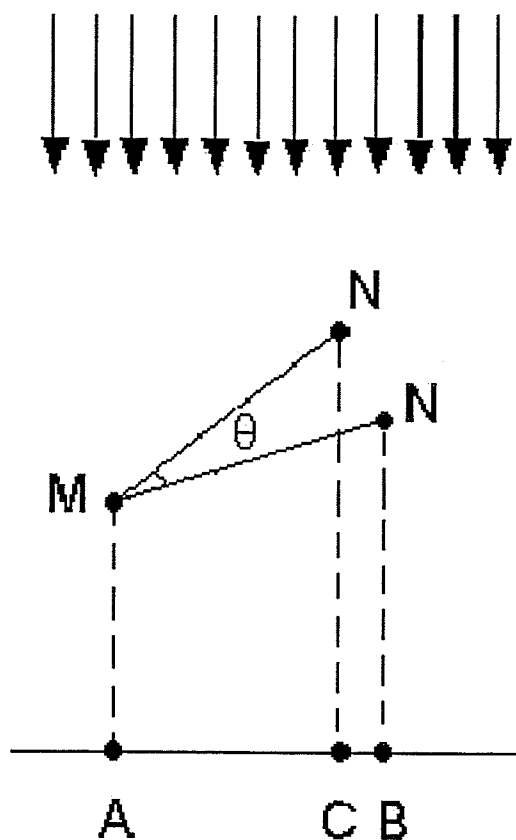
5.5 Discussion

The recovery of out-of-plane rotation is based on registration of anatomical structures. Artificially implanted markers can also be used for image registration with this technique. There are few existing methods for automatic extraction of the artificial landmarks [8-9-13]. After extracting the artificial landmarks from the rest of the portal images it can be used for the recovery of out-of-plane rotation.

Figure 5.12 illustrates an example of this method pertaining to a real clinical case. There are two artificial markers at an “unknown depth”, a fact that is reflective of a real clinical case. One wants to know whether it is possible to use the recovery of the scale factor in order to detect the out-of-plane rotation. The difference between this example and previous approaches is that the previous approaches assume that the landmarks are at the same depth. However in this example the markers are not at the same depth, the fact that arises in many clinical cases.

Provided that we are able to evaluate the distance between the markers, MN , it is possible to recover the scale factor for use in detection of out-of-plane rotation (Eq. 5.1). The distance between the markers can be obtained using CT images [5].

Parallel beams



5.12 Illustration of a case with two markers placed at unknown depths. The image of the object before and after rotation is represented by segments AB and AC.

The second approach is a more realistic representation of the clinical situation, but some situation may arise where the first approach can yield acceptable results. Typical distances for implanted markers could be about 2-5 cm. With respect to the SSD of 100 cm the marker distance of 2 cm corresponds to 2 % so the beam can be assumed to be parallel. One advantage of the first approach, which uses parallel beams, is that the

calculations and equations are much simpler than the second approach. Also the approximations used in Eq. 5.22 in the second approach do not apply to the first approach. On the other hand, the scale factor in the first approach does not depend on the position of the points with respect to each other and it is constant, so it is possible to find a general solution for the scale factor. However, for markers with distances on the order of 20 cm (which corresponds to 20 % for SSD=100), the second approach is more suitable for detection of the out-of-plane rotation.

Another advantage of the FFT based method is that it can detect the difference between out-of-plane rotation and in-plane translation. Figure 5.13 illustrates the geometry of the in plane translation for the second approach. S represents the source and the h is the distance between the object and the source. For an image of the object before translation (A1B1) and after translation (A2B2) we have:

$$\frac{MN}{A1B1} = \frac{h}{SSD} \rightarrow A1B1 = \frac{MN \times SSD}{h} \quad (5.29)$$

$$\frac{MN}{A2B2} = \frac{h}{SSD} \rightarrow A2B2 = \frac{MN \times SSD}{h} \quad (5.30)$$

$$\therefore \frac{A1B1}{A2B2} = 1 \quad (5.31)$$

With in-plane translation there is no change in dimensions of the image, so in-plane translation of the object in the image appears as the magnification factors of unity in both directions.

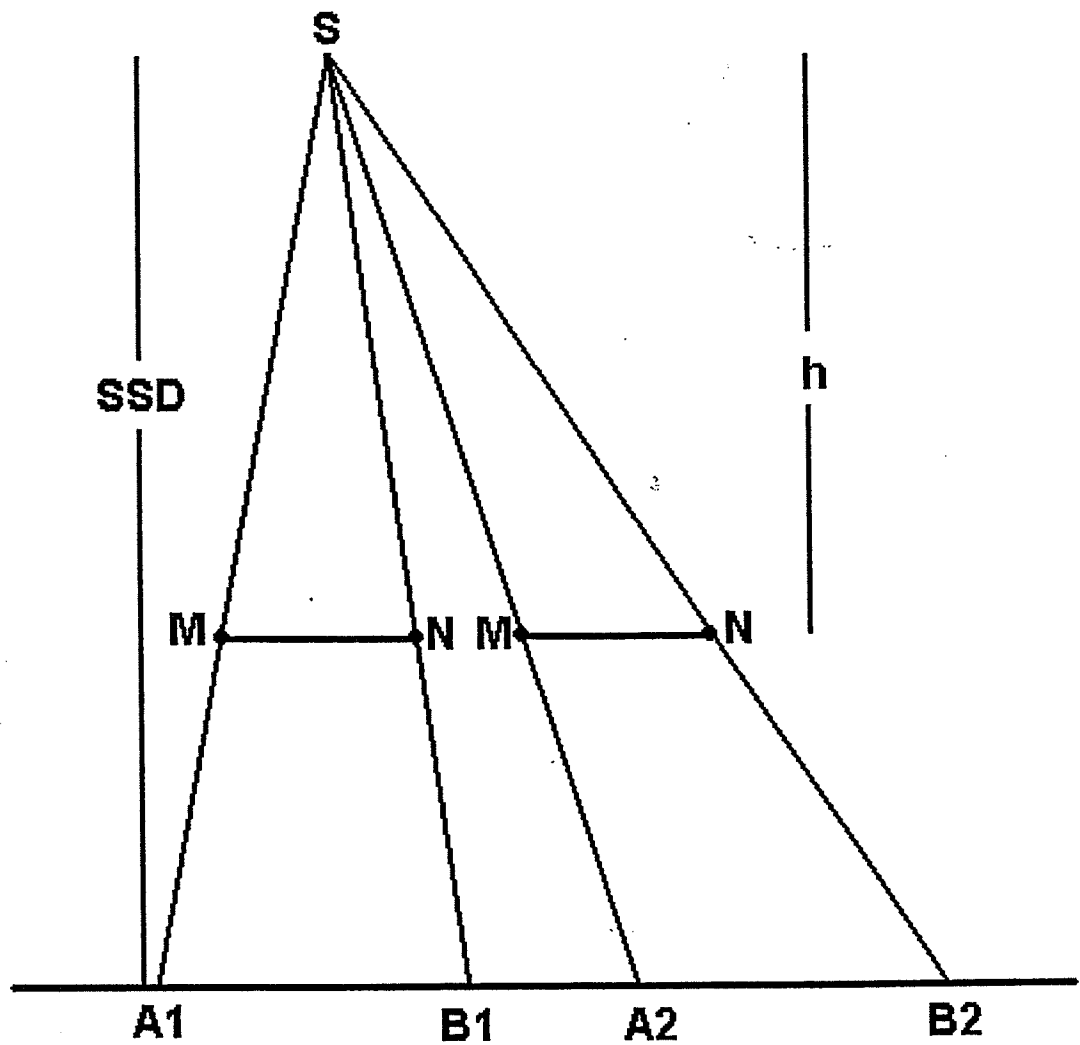


Figure 5.13 The effect of in-plane translation of the object on the size of the image.

The fact that the scale factor is unity in both directions after an in-plane translation is only valid for the points which are located at the same depth. This is illustrated in Figure

5.14. In this example, M and N are two points located at different depths. As we can see, there is a change in the size of the image before and after the out-of-plane rotation (A1B1 and A2B2). However, for the situations that we can apply the first approach, based on the parallel beam approximation, there is no change in the size of the image due to any translation even if the objects are distributed in a volume. So in the first approach we can detect the difference between the in-plane translation and out-of-plane rotation even for the objects located at different depths.

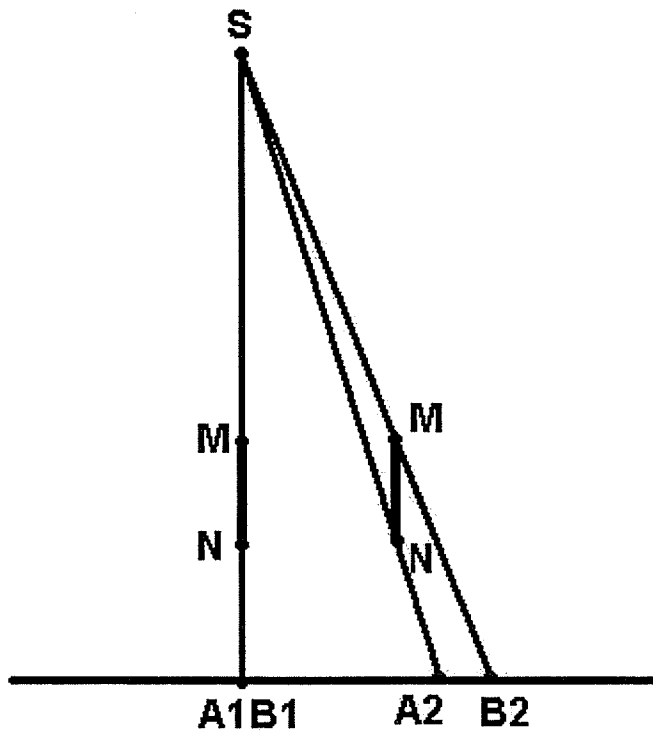


Figure 5.14 The effect of an in-plane translation of the object on the size of the image for two points which are at the different depths.

5.6 References

1. A. Bel, R. Keus, R. E. Vilbrie and J. Lebesque, "Setup deviations in wedged pair irradiation of parotid gland and tonsillar tumors, measured an electronic portal imaging device," *Radiother. Oncol.* **37**,153-159(1995).
2. J. W. Wong, E. D. Slessinger, R. E. Hermes, C. J. Offutt, T. Roy, and M. W. Vannier, "Portal dose images I: Quantitative treatment plan verification," *Int J. Radiat. Oncol. Biol. Phys.* **18**, 1455-1463 (1990).
3. J. Bijhold, M. Van Herk, R. Vijlbrie and J. V. Lebesque, "Fast evaluation of patient set up during radiotherapy by aligning features in portal and simulator images," *Phy. Med. Biol.* **36**, 1665-1679 (1991).
4. J. Hanley, G. S. Mageras and J. Sun and G. J Kutcher, " The effect of out-of-plane rotation on two dimensional portal image registration in conformal radiotherapy of the prostate," *Int. J. Radiation Oncology Bio. Phys.* **33**, 1331-1343 (1995).
5. J. Bijhold, "Three-dimensional verification of patient placement during radiotherapy using portal images," *Med. Phys.* **20**, 347-356 (1993).
6. A. F. Thomton, Jr., R. K. Ten Haken, A. Gerhardsson, and M. Correll, "Dosimetric control "Three-dimensional motion analysis of an improved head immobilization system for simulation, CT, MRI, and PET imaging," *Radiother. Oncol.* **20** 154-162 (1994).
7. M. A. Hunt. G. J. Kutcher, C. Burman, D. Pass, L. Harrison, S. Leibel, and Z. Fuks, "The effect of setup uncertainties on the treatment of nasopharynx cancer." *Int. J. Radiat. Oncol. Biol. Phys.* **27**.437-447 (1993).
8. K. P. Gall and L. J. Verhey, "Computer-assisted positioning of radio-MA- therapy

- patients using implanted radiopaque fiducials," *Med. Phys.* **20**, 1153-1159 (1993).
9. K. L. L. Lam, R. K. Ten Haken, D. L. McShan. and A. F. Thornton, Jr,
"Automated determination of patient setup errors in radiation therapy field using
spherical radio-opaque markers," *Med. Phys.* **20**, 1145-1152 (1991).
 10. X. G. Ding. S. Shalev. and G. Gluhchev. "A technique for verification in
radiotherapy and its clinical applications." *Med. Phys.* **20**, 1135-1143 (1993).
 11. J. Balter, C. A. Pelizzari, and G. T. Y. Chen, " Estimation of extraplanar rotations
for determining patient misalignment in radiation therapy," Proc. AAPM, San
Francisco, *Med. Phys.* **14**, 610 (abstract G3) (1991).
 12. A. F. Thornton, Jr., R. K. Ten Haken, A. Gerhardsson, and A. Correl, "Three-
dimensional motion analysis of an improved head immobilization system for
simulation, CT, MRI, and PET imaging," *Radiother.* **20**, 224-228 (1991).
 13. E. Grusell. A. Montelius, K. R. Russell, E. Blomquist, L. Pellettieri, A.using Lilja,
U. Mostrom, and P. Jakobsson, "Patient positioning for fractionated precision
radiation treatment of targets in the head using fiducial mark-hensive system for
the analysis of portal images," *Radiother. Oncol.* **33**, 68-72, (1994).

6 Conclusion

This thesis has demonstrated that FFT approaches have great potential for the recovery of the translation, rotation, and magnification parameters, which are required to provide image registration for clinical (EPID) images. This technique uses Fast Fourier Transform of the images in log-polar domain for image registration and could be employed as an automatic method for extraction of patient features without the need to define anatomical landmarks or point markers in the portal images. This method considers a large range of frequency for image registration, so it is able to recover the translation parameters within a wide range of variation relative other methods. Morgan's technique is used in this work for the recovery of rotation and scale factor, while the "phase correlation technique" is used for the recovery of translation parameters.

Because of the discrete nature of our data, an interpolation technique for the calculation of the log polar domain is used to create the test images. There are several options for the interpolation method and the "bilinear" method, which is an accurate and fast interpolation method is used in this work.

To reduce sidelobe artifacts, which is a common artifact in the Fourier transform of the finite images a filter is applied to the images before recovery of the transformation parameters. This filter contains a circle with values of zero outside the circle and ones inside.

Using this approach we are able to recover the scale factor, rotation factor and translation factor over the range of 0.86 to 1.28, 0° to 45° and ± 40 pixels with an accuracy of 0.08, 3° and ± 1 pixel respectively. The errors in scale factor recovery are increased for small and larger scales while there is no regular pattern for errors in rotation

recovery versus rotation. The accuracy of the translation recovery was independent of the accuracy in the scale recovery but does depend on the accuracy of the rotation recovery, which needs to be recovered within 5° of accuracy in order to be able to recover the translation parameters.

The second part of this project investigates the possibility of recovering the out-of-plane rotation using a single image. Out-of-plane rotation results in an apparent distortion of anatomy in the portal image, which can be mathematically predicted with the magnification varying at each point in the image. An equal change of magnification in both dimensions results from an incorrect SSD setup, but variation of magnification in only one dimension is due to an out-of-plane rotation. A technique similar to that used for in-plane transforms can be used to calculate the out-of-plane rotation. Correlating the Fourier Transform of the portal image on a log scale with that of the reference image enables the scale factors in two perpendicular directions to be extracted from a single portal image. This is used to automatically recover the out-of-plane rotation using portal images during a treatment session.

One advantage of this method is that it can detect the difference between out-of-plane rotation and in-plane translation, which not possible with existing techniques in portal image registration. The method is based on registration of the anatomical landmarks. One can also use artificial markers (i.e. implanted markers) for image registration using this method.

For the detection of out-of-plane rotation we have taken two approaches. The first approach is based on the assumption that the radiation beams are parallel and the second one assumes that radiation beam is divergent. While second approach is more realistic

there is an approximation in the general solution, which creates an error. If the distance between anatomical structures or implanted markers is small with respect to the SSD, the first approach can be applied for detection of out-of-plane rotation.

This technique is able to identify out-of-plane rotations between 2° and 20° with an accuracy of $\pm 2^\circ$. The ability to detect out-of-plane rotations with a single image will enhance our ability to quickly and accurately account for both in-plane and out-of-plane set-up errors.